



THE UNIVERSITY *of* EDINBURGH

Edinburgh Research Explorer

Wettability Effects on Primary Drainage Mechanisms and NAPL Distribution: A Pore-Scale Study

Citation for published version:

Molnar, IL, Gerhard, JI, Willson, CS & O'Carroll, DM 2020, 'Wettability Effects on Primary Drainage Mechanisms and NAPL Distribution: A Pore-Scale Study', *Water Resources Research*, vol. 56, no. 1, e2019WR025381. <https://doi.org/10.1029/2019WR025381>

Digital Object Identifier (DOI):

[10.1029/2019WR025381](https://doi.org/10.1029/2019WR025381)

Link:

[Link to publication record in Edinburgh Research Explorer](#)

Document Version:

Peer reviewed version

Published In:

Water Resources Research

General rights

Copyright for the publications made accessible via the Edinburgh Research Explorer is retained by the author(s) and / or other copyright owners and it is a condition of accessing these publications that users recognise and abide by the legal requirements associated with these rights.

Take down policy

The University of Edinburgh has made every reasonable effort to ensure that Edinburgh Research Explorer content complies with UK legislation. If you believe that the public display of this file breaches copyright please contact openaccess@ed.ac.uk providing details, and we will remove access to the work immediately and investigate your claim.



Wettability Effects on Primary Drainage Mechanisms and NAPL distribution: A Pore-Scale Study

Ian L. Molnar^{1,4,}, Jason I. Gerhard¹, Clinton S. Willson² and Denis M. O'Carroll^{1,3}*

¹Department of Civil and Environmental Engineering, The University of Western Ontario, London, ON, Canada N6A 5B9

²Department of Civil and Environmental Engineering, Louisiana State University, Baton Rouge, LA 70803

³ now at: School of Civil and Environmental Engineering, Connected Water Initiative, University of New South Wales, Manly Vale, NSW, 2093, Australia

⁴ now at: School of Geosciences, University of Edinburgh, Grant Institute, James Hutton Rd, King's Buildings, Edinburgh EH9 3FE, United Kingdom

*Corresponding author at: School of Geosciences, University of Edinburgh, Grant Institute, James Hutton Rd, King's Buildings, Edinburgh EH9 3FE, United Kingdom. Email address: ian.molnar@ed.ac.uk

14
15
16

17 Key points

- 18 - Water drainage in intermediate wetting system deviated from expected percolation
19 behaviour.
- 20 - Intermediate wetting pores are completely NAPL-filled upon drainage and exhibit no film
21 drainage.
- 22 - NAPL bypassed larger pores more frequently in intermediate wetting sand than in water
23 wetting sand, leaving multi-pore water residual ganglia.

24 Abstract

25 The pore-scale processes governing water drainage behaviour in porous media have implications
26 for geoscience multiphase scenarios including carbon capture and storage, contaminant site
27 remediation, oil recovery, and vadose zone processes. However, few studies report directly
28 observed pore-scale water drainage phenomena in 3-D soils. This knowledge gap limits our
29 ability to verify assumptions underlying existing models and develop optimal solutions. This
30 paper utilizes Synchrotron X-Ray Microtomography (SXCMT) to present an experimental pore-
31 scale examination of non-aqueous phase liquid (NAPL)/water distribution along a primary
32 drainage front as dense NAPL was injected upwards into water-wetting (WW) and intermediate-
33 wetting (IW) sand-packed columns. Pore-network structures were extracted from imaged
34 datasets and mapped onto segmented NAPL/water datasets which allowed quantitative
35 examinations of wettability impacts on (a) the extent to which NAPL fills individual pore bodies,
36 and (b) relationships between pore size and the phase occupying the pore, with both considered
37 as a function of distance (and capillary pressure) relative to the NAPL front. These results
38 revealed that several hypotheses treating IW sand similarly to WW sands are simplistic. IW
39 systems exhibited a sequence of pore filling that deviated from traditional capillary pressure-

40 based model predictions: NAPL invades smaller pores while larger, adjacent pores are bypassed
41 leaving multi-pore residual water ganglia. NAPL pore saturations were close to 1 and did not
42 change with capillary pressure in IW systems. Overall, the results illustrate how a relatively
43 small change in operative contact angle alters NAPL distribution during water drainage, with
44 important implications for geoscience multiphase flow scenarios.

45

46 **1. Introduction**

47 Research into the processes governing multiphase flow is driven by the many relevant
48 applications in groundwater science and engineering. These include: 1) carbon capture and
49 storage systems, 2) groundwater susceptibility to colloid contamination (e.g., viruses or
50 pathogenic bacteria within applied manure) 3) subsurface water balance (e.g., estimating
51 evapotranspiration rates), and 4) remediation technologies and risk assessments for subsurface
52 contamination by non-aqueous phase liquids (NAPLs).

53 Multiphase flow applications are strongly impacted by water drainage processes.
54 Carbon capture and storage (CCS) systems are expected to continuously operate over a period of
55 decades [*Gershenson et al.*, 2017] during which CO₂ displacement of water will dominate. The
56 distribution of pore-scale capillary fringe structures associated with falling groundwater tables
57 (e.g., thin water films, air/water interfaces and pendular rings) impacts the migration of colloids
58 and the rate of subsurface water evaporation [*Wan and Tokunaga*, 1997; *Sirivithayapakorn and*
59 *Keller*, 2003; *Han et al.*, 2006; *Flury and Qiu*, 2008; *Shokri et al.*, 2008; *Shahraeeni and Or*,
60 2010; *Norouzi Rad et al.*, 2013]. The factors governing the remediation and lifespan of dense
61 NAPL (DNAPL)-contaminated sites, such as the ganglia to pool ratio [*Lemke and Abriola*,
62 2006], DNAPL/water surface area [*Bradford and Abriola*, 2001; *Chomsurin and Werth*, 2003]
63 and relative permeability [*Powers et al.*, 1998; *Nambi and Powers*, 2000] are dependent upon
64 NAPL invasion/migration/redistribution.

65 The development of X-ray Computed Microtomographic (XCT) imaging techniques has
66 enabled many recent studies to examine the pore-scale processes governing multiphase flow in
67 natural soils. These XCT studies have focused largely on water imbibition (i.e., the displacement
68 of non-aqueous fluids by water) and the subsequent distribution of non-aqueous fluid residual

69 [e.g., *Al-Raoush et al.*, 2003; *Al-Raoush and Willson*, 2005a; *Schnaar and Brusseau*, 2005; *Han*
70 *et al.*, 2006; *Schnaar and Brusseau*, 2006; *Al-Raoush*, 2009; *Kumar et al.*, 2010; *Iglauer et al.*,
71 2011; *Iglauer et al.*, 2012; *Kumar et al.*, 2012; *Andrew et al.*, 2013; *Chaudhary et al.*, 2013;
72 *Andrew et al.*, 2014a; b; c; *Geistlinger et al.*, 2014; *Geistlinger and Mohammadian*, 2015;
73 *Rücker et al.*, 2015; *Al-Menhali et al.*, 2016; *Singh et al.*, 2016]. In contrast, few experimental
74 XCT studies are available on pore-scale water drainage (i.e., the displacement of water by non-
75 aqueous fluids) within natural soils [*Wildenschild et al.*, 2005; *Culligan et al.*, 2006; *Porter et*
76 *al.*, 2010; *Berg et al.*, 2013; *Herring et al.*, 2013; *Andrew et al.*, 2015b; *Bultreys et al.*, 2015;
77 *Herring et al.*, 2015; *Herring et al.*, 2016].

78 These experimental water drainage XCT studies have yielded valuable insights into the
79 pore-scale processes driving water drainage, extending our understanding of these processes
80 beyond the initial 2-D micromodel studies exploring capillary and viscous fingering [e.g.,
81 *Lenormand et al.*, 1983; *Lenormand et al.*, 1988]. The existence of Haines jumps in 3-
82 dimensional media has since been examined using real-time XCT imaging [*Berg et al.*, 2013;
83 *Bultreys et al.*, 2015]. *Wildenschild et al.* [2005] employed XCT to illustrate how large, well-
84 connected pores drain first. Other XCT studies have examined non-aqueous fluid/water
85 interfacial areas during drainage [*Culligan et al.*, 2006; *Porter et al.*, 2010] as well as how
86 drainage processes can yield small-scale snap-off events [*Andrew et al.*, 2015b]. Pore-scale XCT
87 studies have explicitly linked the distribution of NAPL following drainage with trapping
88 efficiency in CCS systems [*Herring et al.*, 2013; *Herring et al.*, 2015; *Herring et al.*, 2016]
89 showing that hydrophobicity increases the connectivity of the non-aqueous fluid phase and
90 reduces trapping. These XCT studies have been complemented by pore network modeling which
91 has identified additional water drainage mechanisms such as co-operative pore filling [*Holtzman*

92 *and Segre, 2015; Zhao et al., 2016*]. However, a majority of these studies employed systems
93 where water was strongly wetting with respect to the non-aqueous phase; knowledge gaps still
94 exist for drainage in which non-ideal wetting dominates.

95 Wettability significantly affects water drainage and imbibition behavior. Wettability is
96 the preferential spreading of a fluid over a solid surface in the presence of another fluid
97 [*Anderson, 1986b; Powers et al., 1996*] and is quantified by the contact angle formed at the
98 fluid/fluid/solid interface. In this study, contact angle refers to the angle measured through the
99 water phase on a flat surface where $0^\circ < \theta < \sim 60^\circ$ indicates water-wetting (WW) systems, $\sim 60^\circ <$
100 $\theta < \sim 120^\circ$ indicates intermediate-wetting (IW) systems, in which the solid surface has no strong
101 preference for either fluid, and $\sim 120^\circ < \theta < 180^\circ$ indicates NAPL-wetting (NW) systems
102 [*Anderson, 1986a; Powers et al., 1996*]. In addition, porous media may also possess ‘mixed
103 wettability’, which refers to media whose surfaces possess a range of wetting conditions
104 [*Anderson, 1987b*].

105 Wettability is important in the multiphase applications under discussion. Many of the
106 experimental studies exploring pore-scale water drainage processes employed water-wetting
107 media, assuming this was representative of the subsurface. However, numerous studies have
108 illustrated the wide range of scenarios in which the subsurface may be rendered IW. CCS
109 systems may employ oil-reservoir rocks with altered wettability [e.g., *Chaudhary et al., 2013;*
110 *Iglauer et al., 2015*] or the injected CO₂ may render reservoirs IW or weakly WW [*Chiquet et*
111 *al., 2007; Bikkina, 2011; Broseta et al., 2012; Arif et al., 2016; Arif et al., 2017*]. Naturally
112 occurring organic constituents in the subsurface may render the capillary fringe IW [*Ustohal et*
113 *al., 1998; Shokri et al., 2009*]. The wettability of near-surface soils have been modified by forest
114 fires [*Beatty and Smith, 2010*]. NAPL contaminants at brownfield sites may experience a range

115 of wetting conditions due to either additives within the NAPL (e.g., surfactants, anti-oxidants)
116 [Lord, 1999; Hsu and Demond, 2007] or organic components within the subsurface [Ryder and
117 Demond, 2008]. Enhanced oil recovery techniques improve microscopic sweep efficiencies (i.e.,
118 pore-scale oil displacement) by injecting surfactants to deliberately manipulate oil/water/mineral
119 capillary forces [e.g., Kamal et al., 2017] and have noted optimal recovery rates under IW
120 scenarios [Kennedy et al., 1955; Morrow, 1990; Jadhunandan and Morrow, 1995; Hou et al.,
121 2016]. In addition, pore network modeling studies have employed the concept of mixed
122 wettability (either naturally occurring, or deliberately altered via injected surfactants) to describe
123 behaviour observed during waterflooding for oil-recovery [e.g., Kovscek et al., 1993; Blunt,
124 1998; Oren et al., 1998; Dixit et al., 2000; Blunt et al., 2002; Oren and Bakke, 2003].

125 The standard conceptual model of quasi-static water (primary) drainage in water-wetting
126 media generally consists of two dominant pore-body drainage mechanisms: (1) Piston drainage,
127 once an individual pore's displacement pressure (P_d) is exceeded by the local capillary pressure
128 (P_c), non-aqueous fluid rapidly displaces the bulk wetting fluid [Haines, 1930; Melrose and
129 Brandner, 1974; Lenormand, 1986] (i.e., 'Haines jumps'), starting with the largest pore throats
130 (lowest P_d); (2) Film drainage, in which the remaining water surface films, near grain-grain
131 contacts and in small throats, slowly drain via film connections to the bulk wetting phase
132 [Salathiel, 1973].

133 Altered wettability changes the mechanisms driving water drainage. Generally, water
134 drainage occurs at much lower capillary pressures in IW systems because larger contact angles
135 decrease the curvature needed for NAPL to invade a pore throat [Morrow, 1976; Anderson,
136 1987b]. This suggests that for a given P_c , smaller pores will be invaded in altered-wetting
137 systems versus water-wetting. In strongly NAPL-wetting (NW) systems, non-aqueous fluid

138 spontaneously imbibes into pores via films draining the smallest pores first, leaving water
139 residual in the centers of the largest pores [Anderson, 1987a]. However, in IW systems the films
140 are less likely to exist, and the inter- and intra-pore drainage behaviour is less straightforward
141 than in either strongly WW or NW scenarios [Herring *et al.*, 2016]. The disruption of water
142 films in altered wetting media reduces film straining, an important colloid retention mechanism
143 in unsaturated systems, increasing colloid transport [Wan and Tokunaga, 1997; Han *et al.*, 2006].
144 Geologic reservoirs that are either IW or NW will possess lower carbon trapping efficiencies
145 than water-wetting reservoirs [Chiquet *et al.*, 2007; Pentland *et al.*, 2011; Broseta *et al.*, 2012;
146 Iglauer *et al.*, 2012; Krevor *et al.*, 2012; Chaudhary *et al.*, 2013; Krevor *et al.*, 2015; Al-Menhali
147 and Krevor, 2016; Al-Menhali *et al.*, 2016; Alyafei and Blunt, 2016].

148 Current understanding of these drainage mechanisms arises largely from a mixture of
149 theoretical (i.e., mathematical) studies, bench-scale observations, 2-D etched-channel micro
150 models, modelling, and the few XCT studies mentioned previously. There is little experimental
151 data of directly observed pore-scale water drainage processes in 3-D porous media; much of the
152 directly observed pore-scale drainage phenomena are from 2-D micro models [e.g., Lenormand
153 *et al.*, 1983; Lenormand, 1986; Lenormand *et al.*, 1988] with relatively simplistic pore networks
154 and drainage pathways. Key water drainage phenomena identified from 2-D micro-model
155 experiments have not been investigated for 3-D networks, limiting the ability to directly verify
156 their findings for 3-D media and to accurately describe water drainage behaviour in complex
157 multiphase applications in 3-D networks representative of natural soils.

158 The pore drainage order has been indirectly examined in micromodel and XCT studies by
159 comparing the distribution of residual non-aqueous fluids following water re-imbibition to
160 predictions from Percolation Theory. Percolation Theory is a mathematical theory describing the

161 pore-scale distribution of fluids during drainage and imbibition [*Wilkinson and Willemsen*, 1983;
162 *Heiba et al.*, 1986; *Adler and Brenner*, 1988; *Berkowitz and Ewing*, 1998] by mimicking the
163 classic pore drainage order; the invading fluid advances through the medium by invading the
164 most favorable pore/throat at the fluid/fluid interface (i.e., the pore/throat with the lowest
165 capillary pressure threshold) [*Wilkinson and Willemsen*, 1983]. One consequence of this fluid
166 displacement behaviour is that Percolation Theory predicts a power-law distribution of residual
167 ganglia sizes [*Wilkinson and Willemsen*, 1983]; this prediction has been examined by numerous
168 XCT and micro-model pore-scale studies during imbibition [e.g., *Iglauer et al.*, 2011; *Iglauer et*
169 *al.*, 2012; *Georgiadis et al.*, 2013; *Andrew et al.*, 2015a; *Geistlinger and Ataei-Dadavi*, 2015;
170 *Geistlinger et al.*, 2015; *Geistlinger and Mohammadian*, 2015] and water drainage [*Georgiadis*
171 *et al.*, 2013]. While these studies revealed key information about the pore scale behaviour of
172 multiphase-porous media systems they only indirectly examined pore invasion order, whether
173 due to imbibition or drainage processes.

174 Pore-network modeling is similar to percolation theory in concept but with added layers
175 of sophistication. Whereas Percolation Theory models typically assume that a pore is either fully
176 saturated with water or NAPL, pore-network models typically calculate the NAPL pore
177 saturation (i.e., the fraction of a pore body's volume occupied by NAPL) of an invaded pore
178 based on the radius of curvature from the system's capillary pressure [e.g., *Blunt*, 1998; *Oren et*
179 *al.*, 1998; *Blunt et al.*, 2002; *Oren and Bakke*, 2003]. That approach predicts a minimum NAPL
180 pore saturation which depends upon the pore body's geometry [*Blunt et al.*, 2002; *Joekar-Niasar*
181 *and Hassanizadeh*, 2012] which, to the best of the authors' knowledge has never been quantified
182 by experimental observations despite the impact that pore geometry and pore-body saturations
183 have on simulation outcomes.

184 Key knowledge gaps remain in the understanding of multiphase flow through porous
185 media, limiting our ability to ensure optimal outcomes for subsurface multiphase applications.
186 Pore-scale water drainage behaviours are not well understood as most studies have focused on
187 examining residual fluid distributions. Pore-scale water drainage under weakly water-wetting
188 and intermediate-wetting conditions specifically are poorly understood as they have received
189 little attention in the literature [Herring *et al.*, 2016]. There have been no studies quantifying the
190 NAPL pore saturations produced by Haines jumps and how wettability impacts those saturations.
191 In addition, there have been no studies directly quantifying the pore drainage order for either
192 water wetting and weakly water/intermediate wetting scenarios and comparing that to theoretical
193 predictions. Direct observations and quantification of these drainage mechanisms will lead to
194 improved descriptions of pore-scale water drainage mechanisms in pore-network and continuum-
195 scale models, improving outcomes for subsurface multiphase applications.

196 The goal of this study was to improve our conceptual understanding of multiphase flow
197 through soil by filling the knowledge gaps identified above with direct pore-scale, experimental
198 observations of water drainage in water-wetting and intermediate -wetting sands. Synchrotron X-
199 Ray Computed Microtomography (SXCMT) was employed to collect images of NAPL and
200 water distribution during water drainage from two sand-packed columns, one WW and the other
201 IW. This study examined how WW and IW conditions (a) impacted NAPL pore saturations and
202 (b) impacted the relationship between pore size and pore phase occupancy (i.e., the pore is
203 dominated by either NAPL or water). The results reveal how shifting from WW to IW conditions
204 leads to results that deviate from predictions of percolation theory.

205 **2. Materials and Methods**

206 **2.1 Materials**

207 The chemical samples employed in this study, and their method of preparation, followed
208 the procedure described in Molnar et al [2011]. A NAPL/water/surfactant mixture was created in
209 the wet lab in the GeoSoilEnviro Center for Advanced Radiation Sources at Argonne National
210 Lab's Advanced Photon Source approximately 24 hours prior to scheduled beam time. Deionized
211 Ultra Filtered Water (Fisher Scientific) was employed as the aqueous phase. The NAPL used
212 throughout this study was tetrachloroethylene (PCE) (Alfa Aesar, 99%) dyed with 0.25 g/L Oil-
213 Blue-N (Sigma-Aldrich, 96%). The surfactant used to alter the sands' wettability, Dodecylamine
214 (Alfa Aesar, 98+%), was added directly to the PCE at 3.5 g/L. Dodecylamine-in-PCE renders
215 quartz sands intermediate-wetting while leaving iron oxide-coated sands water-wetting at pH
216 values above 6 [Molnar et al., 2011]. The PCE was doped with 1-Iodononane (Alfa Aesar, 97%)
217 at 8% by volume to enhance its contrast with water during SXCMT imaging without
218 substantially changing the wetting properties of the system. A closed glass bottle, containing a
219 1:6.3 PCE:water volumetric ratio was titrated with hydrochloric acid (Fisher Scientific, ACS
220 Grade) to control pH and was allowed to equilibrate on a shaker table for 24 hours. Separate
221 mixtures were created for the quartz and iron oxide drainage experiments; as a result, their pH
222 values vary slightly (quartz mixture: 6.8, iron oxide mixture: 6.7), but not enough to substantially
223 impact their chemical or surface properties. All glassware was thoroughly cleaned using
224 previously described methods [Molnar et al., 2011].

225 The sand employed in this study was a 40/50 Accusand mixture (Unimin, diameter: 300 –
226 420 μ m). The sand was initially acid washed following the procedure of Molnar et al [2011].
227 Approximately half of the sand was set aside as-is for use as an intermediate wetting quartz sand,
228 while the other half was coated with an iron oxide surface coating using the method of Johnson

229 et al. [1996], also used by Molnar et al [2011], so that it would remain water-wetting in the
230 presence of Dodecylamine.

231 The NAPL/water/soil systems examined in this study were chosen to reproduce the
232 wetting conditions quantified by Molnar et al [2011] who measured NAPL/water/solid contact
233 angles for these systems on smooth plates and packed columns of quartz and iron oxide sands
234 (see Table 1). The PCE/DDA samples in that study rendered smooth quartz surfaces strongly
235 NAPL-wetting while smooth iron oxide surfaces remained strongly water wetting. Packed iron
236 oxide sand columns remained strongly water wetting (WW) for iron oxide and but became
237 intermediate wetting (IW) for quartz sand. Throughout this paper we refer to the
238 NAPL/water/quartz sand system as “IW Sand” and the NAPL/water/iron oxide sand system as
239 “WW Sand”.

240 The study presented here assumes that the wetting conditions quantified by Molnar et al
241 [2011] remain directly applicable and are uniform throughout both quartz and iron oxide sands.
242 Johnson et al [1996] reported that the iron oxide coating procedure - the same procedure
243 employed in this study - resulted in a uniform iron oxide coating over the grain surface. It is
244 assumed that the uniform grain coating yields a homogenous wetting condition throughout the
245 iron oxide sand.

246

247 **2.2 Column Experiments**

248 The sands were wet-packed into two small aluminum columns (ID: 5.6 mm, length: 5
249 cm). One column contained quartz sand while the other contained iron oxide-coated sand
250 (referred to throughout this study as IW sand and WW sand, respectively). Water from the
251 water/PCE/surfactant mixture was flushed through each column for at least 20 pore volumes to

252 allow the sand and surfactant to reach equilibrium. Following flushing, the water-saturated
253 columns were securely mounted in the imaging hutch. The PCE mixture was injected upwards
254 using a syringe pump into the column at 200 $\mu\text{L}/\text{min}$ and water was allowed to freely exit the top
255 of the column. The objective was to create NAPL distributions of approximately the same height
256 in the two columns for comparison. The quartz column was imaged at cumulative injected PCE
257 volumes of 100, 150, 300 and 400 μL and the iron oxide column was imaged at 100, 150 and
258 200 μL . These volumes were chosen to yield similar NAPL heights within the columns. The
259 pressure drops during DDA flushing and NAPL injection were not measured. The potential
260 influence of dynamic effects on the NAPL distribution within the columns were estimated by
261 calculating $\tau_s \frac{\delta S_w}{\delta t}$ where τ_s is the damping coefficient estimated from Stauffer [1978] (3.5×10^3
262 $\text{kg}/\text{m}/\text{s}$) and $\frac{\delta S_w}{\delta t}$ is the column-averaged rate of saturation change ($< 0.01 \text{ s}^{-1}$). Given the small
263 $\tau_s \frac{\delta S_w}{\delta t}$ values ($\sim 23 \text{ Pa}$), it is assumed that dynamic effects did not influence the macroscopic
264 drainage behaviour of the WW and IW columns.

265 **2.3 Imaging, Reconstruction and Segmentation**

266 Imaging for this study was conducted at the GSECARS 13BM-D imaging beamline. Imaging
267 was performed above and below the iodine K-edge at 33.27 keV and 33.07 keV so that image
268 subtraction could isolate the iodine-doped NAPL. During imaging the column was rotated 180°
269 while capturing 720 projections at each energy. The image resolution was 10.58 $\mu\text{m}/\text{pixel}$ for the
270 quartz experiment and 10.46 $\mu\text{m}/\text{pixel}$ for the iron oxide experiment. After each flow stoppage,
271 images were collected along 20mm of the column with a 50 pixel overlap so that the
272 reconstructed datasets from each time-step could be stitched together to create a continuous 3-D
273 dataset of NAPL/water distribution along the entire front. Representative vertical cross-sections

274 of all collected and reconstructed datasets are presented in the supplementary information.
275 Approximately 45 – 60 minutes elapsed during each injection and imaging time-step.

276 It is assumed in this study that exposure to x-ray radiation during the imaging process did
277 not alter the wetting behaviour in either system. Brown et al [2014] noted that x-ray radiation
278 could alter the wetting behaviour in three-phase systems through a hypothesized interaction
279 between oil spreading along air/water interfaces and x-ray exposure. The two-phase systems
280 examined here do not possess those three fluid-phase interfaces that led to x-ray wetting
281 alterations. In addition, qualitative examination of the time-lapse images in Figures S1 and S2 in
282 the supplementary information indicate that the wetting behaviours do not change over time (i.e.,
283 with further exposure to x-rays). Previous two-phase XCT studies do not discuss x-ray-induced
284 wetting alterations [e.g., *Al-Raoush*, 2009; *Andrew et al.*, 2014; *Chaudhary et al.*, 2013; *Culligan*
285 *et al.*, 2006; *Han et al.*, 2006; *Stefan Iglauer et al.*, 2015; *S. Iglauer et al.*, 2012; *Porter et al.*,
286 2010] and should be considered an open question for future research.

287 The datasets were reconstructed using a GSECARS-specific reconstruction algorithm in
288 IDL 8.1 (ITT Visual Information Solutions) [*Rivers et al.*, 2010]. Following reconstruction, each
289 voxel in the reconstructed datasets was then segmented into either water, NAPL or solid phases
290 using an indicator kriging method [*Oh and Lindquist*, 1999; *Bhattad et al.*, 2010].

291 Pore-network extraction algorithms [*Thompson et al.*, 2006; *Thompson et al.*, 2008]
292 identified each unique pore along with relevant topological properties (e.g., pore radius, volume,
293 throat sizes) within the reconstructed datasets. The pore-network extraction algorithm
294 [*Thompson et al.*, 2008] defined pore bodies similarly to the common definition of largest
295 inscribed sphere in a pore space region [*Scheidegger*, 1958] but, additionally, employed a burn
296 algorithm to associate pore voxels outside of each inscribed sphere to a pore body. The result is

297 that the pores generated by this extraction algorithm are similar to pore units [e.g., *Sweijen et al.*,
298 2016; *Sweijen et al.*, 2017; *Sweijen et al.*, 2018] as each identified pore body encompasses the
299 entire pore volume between a set of grains as opposed to the pore volume encompassed by the
300 largest inscribed sphere. Throats are also defined in a similar manner to pore units, as the facet
301 area between two pore bodies and contain no volume. However, unlike the pore unit generation
302 approach, this algorithm does not rely on assumptions regarding grain packing arrangements
303 (e.g., tetrahedral) or pore body geometry. Figure 1c illustrates the distribution of uniquely
304 identified pore bodies generated by this extraction algorithm from a representative 2-D slice.

305 The segmented NAPL/water datasets were then mapped onto the extracted pore-network
306 to correlate network structure with NAPL/water phase distribution. Previous studies have
307 reported that the ratio of resolution of grain diameter employed within this study is sufficient to
308 accurately quantify and resolve the pore-network structure [*Al-Raoush et al.*, 2003; *Al-Raoush*
309 *and Willson*, 2005a; b].

310 **3. Results and Discussion**

311 **3.1 Pore-network characterization**

312 Table 2 presents an overview of extracted topological and pore-network characteristics.
313 The SXCMT-determined porosities differ between the WW and IW datasets, but otherwise the
314 pore network characteristics are generally consistent. Figure 1a illustrates that the distribution of
315 WW and IW pore inscribed radii (PIR) are similar but not identical; the WW sand has a slightly
316 higher percentage of large pores. The higher number of large WW pores corresponds to a higher
317 number of pores with radii between 0.01 and 0.014 cm relative to the IW sand and accounts for
318 the difference in porosity (see Figure S3 in the supplementary information). Despite differences

319 in pore size distribution, Figure 1b reveals that the distribution of pore throat sizes is almost
320 identical between the two sands.

321 Given the consistency between the IW and WW pore networks and pore throat size
322 distributions – which control NAPL entry into pore bodies – we have a high degree of
323 confidence in comparing DNAPL distribution between the two networks. Specifically, the
324 analyses presented within this paper focuses on whether individual pores are occupied by water
325 or NAPL, the influence of pore size on that phase occupancy, and quantifying NAPL saturation
326 within individual pore bodies. As a result, ensuring that the size and shape characteristics of
327 individual pores are comparable between the two datasets is crucial and Table 2, Figure 1 and
328 Figure S3 demonstrate that both datasets have a similar number of pores, similar number of
329 throats, similar pore connectivity's and span the same range of pore inscribed radii.

330 **3.2 Macroscopic NAPL Saturation Trends**

331 Vertical cross-sections of the fluid distribution in the 150 μ L WW and 200 μ L IW
332 datasets are presented in Figure 2a and 2b along with magnified views of a portion of the cross-
333 sections in Figure 2c and 2d. Cross-sectional views of all collected WW and IW datasets are
334 presented in Figures S1 and S2, respectively, in the Supplementary Information. The two
335 datasets were chosen for comparison as their NAPL invasion fronts reach approximately the
336 same height in both columns. In Figures 2a and 2b, the injected NAPL was present up to
337 between 1.8 and 1.9 cm from the base of the image.

338 Within the WW sand, pores appear to contain both NAPL and water, with water
339 remaining in the throats and at grain-grain contacts (Figure 2d). In the IW sand, water residual

340 appears to be in larger, connected ganglia (Figure 2c) with little water in pores that have been
 341 invaded by NAPL.

342 The qualitative observations of residual water structures in Figure 2 are similar to Han et
 343 al [2006] who examined the distribution of residual water structures with XCT and noted larger
 344 multi-pore water ganglia in mixed wetting systems. Similarly, Al-Menhali et al. [2016] noted
 345 that residual CO₂ structures also favored larger, multi-pore ganglia in mixed-wetting systems.
 346 Bench-scale experimental studies of scCO₂ trapping have hypothesized the formation of large,
 347 multi-pore residual ganglia in intermediate-wetting systems [e.g., *Alyafei and Blunt, 2016*];
 348 however, this has never been confirmed. They further proposed pore-bypassing as the
 349 mechanism responsible for generating these residual structures. In pore-bypassing, an invading
 350 fluid surrounds a cluster of pores occupied by the draining fluid, cutting the draining fluid off
 351 from the surrounding pores and generating large multi-pore residual fluid ganglia. The large
 352 water ganglia observed in the IW sand in Figure 2a and 2c supports the hypothesis that
 353 intermediate wetting systems will also form large, multi-pore structures during drainage.

354 The relative strength of capillary forces are described using the Capillary (Ca) and Bond
 355 (Bo) numbers, defined respectively as the ratios of viscous to capillary and gravity to capillary
 356 forces. Ca and Bo values were estimated from Eq.'s 1 and 2 [*Dawson and Roberts, 1997*;
 357 *Herring et al., 2016*]:

	$Ca = \frac{v_N \mu_N}{\gamma_{NW} \cos \theta}$	Eq. 1
	$Bo = \frac{\Delta \rho g d^2}{\gamma_{NW} \cos \theta}$	Eq. 2

358 Where v_N is the pore water velocity of the injected NAPL, μ_N is the viscosity of the NAPL, γ_{ow}
359 is the interfacial tension of the NAPL-water interface, θ is the contact angle, $\Delta\rho$ is the difference
360 in density between the NAPL and water phases, g is the gravitation constant and d is the average
361 grain diameter. These relationships are only valid for the contact angle range of $0 < |\theta| < 90^\circ$. The
362 estimated Ca numbers, using the relationship from Dawson and Roberts [1997], are 6.3×10^{-5} and
363 2.9×10^{-5} for the IW and WW sands, respectively. The Bo numbers, estimated using a relationship
364 from Herring et al. [2016], are 0.14 and 0.064 for the IW and WW sands, respectively. The
365 differences in Ca and Bo numbers are solely due to the change in wettability. While contact
366 angles were not measured directly within the XCT images, the change in wettability was
367 quantified from the operative contact angles (i.e., contact angles derived by Leverett-scaling
368 capillary pressure-saturation relationships, measured through the water phase) reported in
369 Molnar et al [2011] as 0° for the water wetting (iron oxide) sand, and 63° for the intermediate
370 wetting (quartz) sand. These numbers reveal that the IW sand has weaker capillary forces
371 relative to the WW sand.

372 **3.3 Pore Body NAPL Saturation Trends**

373 Piston drainage, the NAPL invasion event that occurs when the system's capillary
374 pressure exceeds the pore body's entry pressure, has been studied both within pore-network
375 modeling [e.g., Blunt, 1998; Oren et al., 1998; Blunt et al., 2002; Oren and Bakke, 2003] and
376 experimentally within complex 3-D media [Berg et al., 2013; Bultreys et al., 2015]. This section
377 examines the NAPL saturations within individual pore bodies in the 150 μL WW and 200 μL IW
378 datasets introduced in Section 3.2.

379 Figures 3a and 3b plot the measured NAPL pore saturations for each pore in the WW and
380 IW sands as a function of the pore's height from the base of the column. Both columns were

381 identical, images were collected at same distance from the outlet (3 cm from the column outlet)
382 in both WW and IW systems. The observations are in general agreement with the pore-network
383 modeling predictions that piston drainage generates a minimum NAPL pore saturation. While a
384 range of NAPL pore saturations are observed in both WW and IW sands, most pores either had
385 essentially no NAPL (<0.05) or a high NAPL pore saturation (>0.8). In both WW and IW sands,
386 high NAPL saturations occurred regardless of the pore's location along the NAPL front. Even
387 pores at the very leading edge of the front had high saturations, suggesting that Haines jumps
388 rarely produce pores with low NAPL saturations.

389 Classical water drainage theory for water wetting conditions suggests that NAPL pore
390 saturations should increase with capillary pressure as the radius of curvature decreases, allowing
391 water to drain from the corners of the pore [Blunt *et al.*, 2002]. Measured NAPL pore saturations
392 within the WW sand (Figure 3a) slowly increase with distance from the leading edge of the
393 NAPL front (i.e., from top to bottom in the column). This agrees with the prediction that pores
394 experience both an initial invasion event followed by the slow, film drainage of water. The
395 measured NAPL pore saturations within the IW sand (Figure 3b) are higher than WW pore
396 saturations at the base of the image (WW: 0.86, IW: 0.92) and change more gradually with
397 distance from the leading edge of the NAPL invasion front (slope of fitted trendlines in Figure 3,
398 WW: -0.037, IW: -0.015). This suggests that while both WW and IW pore bodies experience an
399 initial invasion event, the IW pore saturation changes minimally with higher capillary pressures
400 (i.e., little film drainage occurs).

401 Pore network modeling studies of oil reservoir rocks [e.g., Dixit *et al.*, 1996; Blunt, 1998;
402 Oren *et al.*, 1998; Dixit *et al.*, 2000; Blunt *et al.*, 2002; Oren and Bakke, 2003] typically
403 incorporate wettability changes (i.e., NW or IW systems) using a model proposed by Kovscek et

404 al [1993]. This model suggests that pores are initially water-wet during water drainage (i.e.,
405 during the initial Haine's jump). As the NAPL saturation increases within the pore due to film
406 drainage, NAPL will contact the solid surface and change the wettability at that location to either
407 IW or NW, eliminating water films at those contact points. Moreover, this approach predicts an
408 increase in NAPL pore saturation with increasing capillary pressure similar to that predicted (and
409 here observed) for WW sand. However, since Figure 3b illustrates that the NAPL pore
410 saturations change more gradually with height than WW systems, this pore-network modelling
411 approach for draining IW/NW pores is not applicable to the IW system explored in this study.
412 The trends in Figure 3b suggest that the surfactant renders pores intermediate wetting prior to
413 drainage. This difference between pore-network prediction and experimental observation for IW
414 sand is likely due to the column packing/preparation process employed in this study where the
415 IW sand was initially flushed with surfactant, rendering it intermediate-wetting prior to water
416 drainage.

417 The differences in NAPL pore saturations between the WW and IW sands are further
418 quantified in Figure 4 for specific regions within the column. While Figures 3a and 3b illustrate
419 how NAPL pore saturations change with distance from the NAPL invasion front (i.e., from top to
420 bottom in the column), Figure 4 directly compares the distribution of NAPL pore saturations
421 between WW and IW wetting conditions. Considering only the pores that contained NAPL (i.e.,
422 NAPL pore saturations > 0), the NAPL pore saturation distributions exhibit a high degree of
423 skewness, with the highest % of pores at very high NAPL pore saturations. In the IW sand, the
424 highest percentage of NAPL-occupied pores were at NAPL pore saturations of 98% (top), 100%
425 (middle) and 100% (bottom). In the WW sand, the highest percentage of pores had NAPL pore
426 saturations of 88% (top), 89% (middle) and 92% (bottom). This confirms the identified shift

427 towards higher NAPL saturations at greater distances from the NAPL invasion front (and higher
428 capillary pressures) in the WW sand, a trend that is not observed in the IW sand.

429 The above results generally confirm that NAPL invasion can be treated mainly as a
430 binary event: a pore is either highly saturated with NAPL or water. Few pores possess pore
431 saturations between those extremes. In the IW sand: 16.8% of pores have NAPL pore saturations
432 < 0.05 and 74.7% of pores have NAPL pore saturations > 0.75 , while only 8.5% of pores have
433 saturations in between. Similarly, for the WW sand: 27.5% of pores have NAPL pore saturations
434 < 0.05 and 57.9% of pores have NAPL pore saturations > 0.75 , while only 14.6% of pores have
435 saturations in between.

436 **3.4 Pore Phase Occupancy Trends**

437 Classical water drainage in a uniformly water-wetting sand is expected to first occur in
438 the largest pores (i.e., lowest displacement pressure), followed by medium sized pores, with the
439 smallest pores either draining last or remaining occupied by residual water [e.g., *Lenormand et*
440 *al.*, 1983; *Blunt*, 1998; *Fenwick and Blunt*, 1998; *Oren et al.*, 1998; *Blunt et al.*, 2002; *Oren and*
441 *Bakke*, 2003]. This section examines the impact of wettability on this water drainage order by
442 linking phase occupancy of a pore with the characteristics of individual pore bodies for the 150
443 μL WW and 200 μL IW datasets discussed in Sections 3.2 and 3.3. For the purpose of this study,
444 a NAPL-occupied pore is defined as any uniquely-identified pore that has a NAPL pore
445 saturation greater than 20%. Conversely, a water-occupied pore is defined as a uniquely
446 identified pore with a NAPL saturation less than 20%. Given that few pores possess NAPL pore
447 saturations between 0.05 and 0.75, the saturation threshold chosen to define whether a pore is
448 NAPL- or water-occupied has little impact on any analysis of pore phase occupancy trends.

449 The following analysis focuses on examining water drainage as a function of pore size.
450 However, in water drainage scenarios it is throat size, not pore size, that controls the pore's
451 drainage behaviour. Due to the complex structure of the two porous media examined in this
452 study and the static nature of time-lapse XCT imaging, it is infeasible to identify which throat
453 controlled the drainage behaviour of each pore and assess pore phase occupancy on that throat's
454 inscribed radii. The analysis presented depends on correlation between pore body size and pore
455 throat size. This correlation is valid for these sands, as demonstrated by Figure 5. It is
456 acknowledged that this may not be the case for all porous media, and that this relationship
457 involves some scatter associated with pore structure heterogeneity.

458 It should be noted that the capillary numbers for WW and IW are outside the range of
459 applicability for Percolation Theory ($Ca < 10^{-6}$) [Geistlinger *et al.*, 2015]. As a result,
460 quantitative predictions from Percolation Theory (e.g., power-law predictions of residual ganglia
461 size) are not applicable to this study. However, capillary forces still dominate the drainage
462 behaviour of both systems and the classic pore drainage order is still expected. In addition to the
463 macroscopic Capillary number discussed in Section 3.2 , the ratio of viscous to capillary forces
464 at the pore-scale was calculated utilizing the method of Blunt and Scher [1995] which
465 incorporates throat length (average throat length, WW: 0.28 mm, IW: 0.25mm) and throat radius
466 (average throat radius, WW: 0.032 mm, IW: 0.030) to yield a viscous/capillary force ratio of
467 0.03 and 0.05 for the WW and IW systems, respectively. Thus, while pore-scale viscous forces
468 are non-zero in both systems, this force ratio suggests that capillary forces govern pore-scale
469 water drainage. While it is unlikely that the differences in capillary numbers (discussed in
470 section 3.2) and pore-scale force balances between the IW and WW sands represent a shift from

471 capillary- to viscous-dominated flow, the following analysis does rely on the assumption that
472 both systems are capillary-force dominated.

473 The effect of wettability on pore occupancy sequence for the WW and IW sands are
474 presented in Figures 6a and 6b where NAPL- and water-occupied pores are plotted as a function
475 of PIR and height. Only water-occupied pores adjacent to at least one NAPL-occupied pore were
476 included in the figures; therefore, these figures present pores that remained water-occupied due
477 to their geometry rather than simply being far from the NAPL front. In these figures, the bottom
478 region possesses the highest capillary pressures while the top represents the leading edge of the
479 NAPL invasion front. For this discussion, large pores have $PIR > 0.01$ cm, medium pores have
480 $0.005 \leq PIR \leq 0.01$ cm and small pores have $PIR < 0.005$ cm. A sensitivity analysis presented in
481 Figure S4 in the supplementary information demonstrates that the pore phase occupancy
482 presented in Figures 6a and 6b is insensitive to the chosen NAPL saturation threshold.

483 The phase occupancy trends observed in Figure 6a for the WW sand confirms the classic
484 water drainage sequence: NAPL first invaded the largest pores (1.4 – 1.8 cm height) followed by
485 medium-sized pores (0.8 – 1.2 cm height), and the smallest pores remained water-occupied at all
486 heights. There is a strong separation in Figure 6a between the radii of NAPL-occupied and
487 water-occupied pores. Some deviations from classic water drainage theory exist: 9% of small
488 pores are NAPL-occupied in the WW sand while ~1% of large pores remained water-occupied.
489 However, the large water-occupied pores were all at the top of the column, suggesting they
490 would eventually be invaded by NAPL. This suggests that pore body radius is a strong, but
491 imperfect, predictor of NAPL invasion in water-wetting porous media.

492 The predicted drainage order for IW sands is less clear, but is expected to be less
493 dependent upon pathway size (i.e., pore size) than WW media [Herring *et al.*, 2016]. However,

494 pore-network modelling studies of water drainage in IW systems typically assume a drainage
495 order consistent with Percolation Theory (i.e., pores with lowest capillary pressure still drain
496 first) [e.g., *Blunt*, 1998]. In intermediate wetting systems with $\theta < 90^\circ$ (i.e., positive capillary
497 pressures), this assumption predicts a pore drainage order similar to WW systems. However, this
498 assumption has not been tested through observation of 3-D experimental pore-scale systems.

499 The IW sand's measured pore occupancy sequence (Figure 6b) illustrates that pore
500 inscribed radius is not as strong a predictor of pore phase occupancy in IW sand as it is in the
501 WW sand. The IW sand's drainage order does not exhibit the strong pore size differentiation
502 between NAPL-occupied and water-occupied pores observed in the WW sand. As in the WW
503 sand, the largest pores are still NAPL-occupied and the smallest pores are water-occupied.
504 However, a large overlap of NAPL-occupied and water-occupied pore radii exists relative to the
505 WW sand (i.e., more medium sized pores remained water-occupied). A total of 2% of the large
506 pores with radii $> 0.01\text{cm}$ remained water occupied in the IW sand, similar to the WW sand
507 ($\sim 1\%$). However, larger water occupied pores were observed in the IW sand even near the base
508 of the column where water appears to be at residual macroscopic saturation (Figure 2). As a
509 result, the observed pore occupancy sequence in the IW sand deviates from the expected water
510 drainage order. Figure 6 indicates that NAPL is more likely to bypass medium and large-sized
511 pores in the IW sand than in the WW sand. This NAPL by-passing phenomenon can be
512 qualitatively observed in the cross-sectional image of the IW sand Figure 2a. A single, large
513 water ganglion can be seen between 0.4 and 0.8cm from the bottom of the column.

514 The wettability induced-deviations from classic water drainage behaviour is further
515 quantified in Figure 7 for three distinct regions in the NAPL front: bottom of the column (0.2-
516 0.6cm from the base), middle of the column (0.8-1.2cm) and top of the column (1.4-1.8 cm from

517 base). Specifically, Figure 7 presents the percentage of pores occupied by a phase vs inscribed
518 radius of the pore along with the associated total filtered pore size distribution for each specific
519 height interval while Table 3 summarizes the phase occupancy trends in terms of large, medium
520 and small pores.

521 Some deviations from the drainage order of large > medium > small pores are expected.
522 Complex pore-structures, connectivities and topology can lead to the drainage of smaller pores
523 with higher entry pressures prior to larger pores and both Percolation Theory and pore-network
524 models implicitly account for this [e.g., *Blunt et al.*, 2002]. This behavior is observed throughout
525 both WW and IW sands. Within the top region of both WW and IW sands – where capillary
526 pressures are lowest – NAPL occupies a wide range of pore radii (WW: 0.001-0.017cm, IW:
527 0.003-0.016 cm) with an overlapping range of water-occupied pore radii (WW: 0.001 – 0.011
528 cm, IW: 0.001 – 0.016 cm). This indicates that NAPL can invade smaller pores prior to larger
529 pores, regardless of the wettability. However, this also illustrates that NAPL bypasses more of
530 the larger water-occupied pores in the IW sand than the WW sand within the top region. This
531 trend extends throughout the dataset: NAPL bypassing of medium- and large-sized pores in the
532 IW sand can also be seen in the range of water-occupied pore radii in the middle region (WW:
533 0.001 – 0.008 cm, IW: 0.001 – 0.01 cm) and at the bottom where capillary pressures are the
534 highest (WW: 0.001 – 0.006 cm, IW: 0.001 – 0.01 cm).

535 The similarity of the WW and IW pore-network statistics (e.g., pore and throat size
536 distribution) suggests that these differences in pore occupancy sequence and NAPL bypassing
537 are driven by differences in wettability. For example, in the middle region, 13% of small IW
538 pores are invaded by NAPL before the remaining 12% of medium pores. In contrast, there is
539 little overlap in pore size vs phase occupancy for the WW sand. In the middle region, 12% of

540 small WW pores are invaded with only 2% of medium pores remaining. Examining the top
541 region produces similar conclusions.

542 The mechanism driving the increased magnitude of NAPL bypassing in the IW sand is not
543 revealed by these data. One potential cause may be that the IW sand became fractionally wetting
544 following pre-equilibration with the surfactant, instead of achieving a uniform intermediate
545 wetting condition.

546 In this study, interactions between the positively charged surfactant (Dodecylamine) and
547 mineral surfaces (quartz, iron oxide) controlled the wettability of the system. This rendered the
548 negatively charged quartz surface intermediate wetting while the positively charged iron oxide
549 remained water wetting. A heterogeneous distribution of mineral surface charges and adsorbed
550 surfactant might render the surface fractionally wet. The point of zero charge of the iron oxide
551 sand (6-8) [Molnar *et al.*, 2011] is close to the pH of the system (6.7), thus a heterogenous
552 distribution of positive and negative surface charges and Dodecylamine absorption could be
553 expected. However, the iron oxide system exhibited strongly water wetting behaviour throughout
554 this study, with the classical water wetting pore occupancy sequence and gradual drainage of
555 water from pore bodies following the initial invasion event, suggesting that it was not
556 fractionally wetted. The point of zero charge of quartz (2) [Molnar *et al.*, 2011] is far from the
557 pH of the system (6.8) and is expected to be predominantly negatively charged, suggesting that
558 fractional wettability could not arise from a variation in surface charges. Mineral heterogeneity
559 on the quartz sand surface, leading to a heterogeneous distribution of surface charges and
560 surfactant adsorption, is also an unlikely cause of fractional wettability as the quartz (IW) sand in
561 this study was a high purity silica sand [Schroth *et al.*, 1996].

562 Another possibility is that viscous forces are responsible for the deviations from the
563 expected pore drainage order in the IW sand. However, the differences between the
564 viscous/capillary force ratios for the two systems is small (macroscopic-scale capillary numbers:
565 2.9×10^{-5} vs 6.3×10^{-5} for the WW and IW systems respectively) relative to the observed
566 differences in pore drainage order. Further work is required to elucidate the mechanisms driving
567 deviations from the expected drainage order in the IW system and should focus on examining IW
568 drainage across a range of capillary and mobility numbers.

569 An analysis of the total pore size distributions for each height interval in Figure 7 is also
570 unable to explain the bypassing trend. The IW system does have a higher percentage of medium-
571 sized pores (PIR: 0.005 – 0.01 cm) than the WW system in the top interval. However, the middle
572 and bottom height intervals have comparable pore size distributions between the WW and IW
573 datasets – pore size distributions are generally bi-modal in both WW and IW systems, with
574 peaks occurring at similar inscribed radii values and with similar percentages – and still exhibit
575 bypassing behaviour (see Table 3).

576 The formation of large ganglia in intermediate wetting scenarios similar to that seen Figure
577 3a has been observed during drainage from 2-D micromodel cells [e.g., *Zhao et al.*, 2016]. It is
578 difficult to compare the bypassing events observed in Figures 5b and 6b to literature observations
579 due to a lack of reported pore sizes and discussion of the phenomena.

580 A likely explanation for the IW bypassing behaviour is the simultaneous existence of
581 concave and convex curvatures across fluid/fluid interfaces that exist in mixed-wetting [*Blunt et*
582 *al.*, 2019] and uniformly intermediate wetting [*Rabbani et al.*, 2017; *Rabbani et al.*, 2018]
583 scenarios. In addition, curvatures may flip between concave and convex when interfaces moving
584 through converging and diverging intermediate-wetting pore throats [*Rabbani et al.*, 2018]. Thus

585 a range of apparent wettabilities can exist within even uniformly intermediate wetting media
586 leading to a distribution of positive and negative capillary pressures that changes across time and
587 space. Rabbani et al [2017] noted the distribution of concave and convex curvatures led to
588 pinned interfaces in scenarios where the interface was expected to advance across a pore body,
589 and also to invading fluids withdrawing from already-invaded pores. Such behaviour would be
590 expected to lead to the pore bypassing observed in the IW datasets examined here.

591 While it is not possible to definitively link the distribution of NAPL/water observed in the
592 IW scenario here to interface curvature dynamics, it does represent the most likely explanation.
593 Developing further understanding of these multipore bypassing events is especially important as
594 they are expected to govern CO₂ trapping in intermediate wetting systems [*Alyafei and Blunt,*
595 2016], increase the rate at which colloids and viruses migrate through the vadose zone [*Han et*
596 *al., 2006*] and impact key parameters such as relative permeability which control the rate of
597 NAPL dissolution at contaminated sites [*Phelan et al., 2004*] and the efficiency of water
598 flooding for oil recovery [*Blunt, 1998*].

599

600 **Conclusions**

601 The presented results provide new, direct observations of how water wetting and
602 intermediate wetting conditions can affect the pore-scale distribution of NAPL during water
603 drainage. This work addressed several key knowledge gaps (e.g., pore drainage order in weakly
604 water wetting sands, saturations produced by Haines jumps) with direct experimental pore-scale
605 observations. In so doing, it is now possible to evaluate several hypotheses proposed by pore-
606 scale modelling and bench scale studies. In several cases, the data confirms existing theories.

607 For example, the data supports the fact that capillary forces, relative to viscous and gravity
608 forces, are reduced in intermediate wetting systems compared to water wetting systems.
609 Moreover, these observations substantiate that, regardless of wettability, pore-body filling is
610 mainly a binary event (either water or NAPL-occupied) with few pores exhibiting intermediate
611 NAPL pore saturations.

612 However, in several areas, the data suggests that existing conceptual models – which have
613 historically focused on water- and NAPL-wetting conditions – do not fully describe the
614 intermediate wetting scenario examined here and require further development. For example, at
615 the scale of a single pore body, the typical mechanisms of water drainage under water wetting
616 conditions are generally assumed to be piston displacement followed by film drainage as P_c
617 increases. The NAPL pore saturation distributions quantified in this work support this model for
618 water-wetting systems. For this intermediate wetting system, these results suggest instead that
619 many residual water structures such as pendular rings, bridges, and water in corners of grain-
620 grain contacts were disrupted by grain-surfactant interactions.

621 For another example, the standard conceptual model of water drainage suggests that NAPL
622 initially invades the largest pores, followed by increasingly smaller pores as the capillary
623 pressure of the system increases, and this is assumed for both water-wetting and intermediate-
624 wetting systems. The measurements presented here indicate that this drainage order was
625 supported for water-wetting media. However, the intermediate wetting system examined
626 demonstrated deviations from this standard behaviour, increasing the likelihood of NAPL
627 bypassing larger pores, generating multi-pore water ganglia. The mechanisms governing the
628 observed wettability-induced NAPL distribution may well be due to bypassing mechanisms or

629 co-existing concave and convex NAPL/water interfaces, but this data cannot confirm those
630 related hypotheses.

631 When pore-phase occupancy and pore-body saturation trends are considered together, the
632 impact of wettability alterations on pore-scale water drainage is not straightforward. There are
633 changes to drainage mechanisms of individual pore bodies as well as changes to the processes
634 occurring at the scale of the pore network. The changes observed in the intermediate-wetting
635 sand's pore drainage sequence could lead to deviations from pore network model predictions
636 based upon classic invasion percolation assumptions.

637 It is acknowledged that our experimental results are discussed in the context of a conceptual
638 understanding of percolation theory. This understanding has emerged from numerous pore
639 network modelling studies, which rely on numerous assumptions and are generally developed for
640 consolidated porous media. Hence, it may not be entirely fair to compare our results to this
641 understanding so developed. However, this does not alter the fact that our observations are novel
642 and unlike standard expectations.

643 These results have implications for intermediate-wetting scenarios. The disrupted residual
644 water structures and the corresponding high pore body NAPL saturations will likely increase
645 colloid and virus transport through the vadose zone, as residual water structures are a significant
646 colloid retention mechanism. Similarly, the changes in pore occupancy sequence, especially the
647 increased numbers of water-occupied medium sized pores, will also increase the mobility of
648 colloids in the vadose zone. NAPL degradation/dissolution processes will be impacted by both
649 the loss of residual water structures within individual pores and the generation of larger multi-
650 pore water ganglia which will change both the relative permeability and the NAPL-water
651 interfacial area, altering interfacial mass transfer rates. Likewise, the removal of residual water

652 structures during scCO₂ injection could eliminate CO₂ snap-off and subsequent capillary trapping
653 during water flushing, leaving the poorly understood process of pore by-passing and multi-pore
654 ganglia generation as the predominant trapping mechanisms. In addition, the high pore body
655 saturations in the intermediate wetting sand could lead to the observed higher pore filling and
656 macroscopic sweep efficiencies for enhanced oil recovery under intermediate wetting conditions
657 [e.g., *Kennedy et al.*, 1955; *Jadhunandan and Morrow*, 1995].

658 The pore-scale observations presented here could be employed to improve descriptions of
659 multiphase flow in both pore-network and continuum models. For instance, incorporating the
660 processes presented here into pore network models would improve their accuracy for
661 intermediate wetting scenarios. As relative permeability models, in the absence of experimental
662 data, often rely on data generated by pore network models, improving the accuracy of pore
663 network model outputs would improve continuum multiphase flow models. Building the pore-
664 level observations presented here into both pore network models and conceptual models would
665 improve model descriptions of hysteresis as both pore occupancy sequences and intra-pore water
666 distributions following drainage impact imbibition pathways and snap-off/capillary trapping
667 behaviours.

668 Many of the existing pore-network models developed for intermediate wetting scenarios rely
669 on the assumption that wettability only changes after water drains from a pore whereas these
670 results highlight how wettability change can occur before drainage in certain circumstances.
671 Pore-network models would benefit from incorporating this pre-drainage wetting alteration.
672 Overall, these results point to unique multiphase flow behaviour in intermediate wetting
673 scenarios that should be considered when developing and applying computational models.

674 It is worth reiterating that these changes were all observed with a relatively small change in
675 operative contact angle, suggesting that only small changes in porous media wettability are
676 needed to influence the water drainage behavior, and NAPL distribution, for a wide range of
677 important multiphase systems.

678 **Acknowledgements**

679 We acknowledge the support of GeoSoilEnviroCARS (sector 13), which is supported by the
680 National Science Foundation– Earth Sciences (EAR-1128799) and the Department of Energy–
681 Geosciences (DE-FG02-94ER14466). Use of the Advanced Photon Source, an Office of Science
682 User Facility operated for the U.S. Department of Energy (DOE) Office of Science by Argonne
683 National Laboratory, was supported by the U.S. DOE under contract no. DE-AC02-06CH11357.
684 This research was supported by the Natural Sciences and Engineering Research Council
685 (NSERC) of Canada. Portions of this research (pore network extraction and image segmentation)
686 were conducted with high-performance computing resources provided by Louisiana State
687 University (<http://www.hpc.lsu.edu>). The datasets presented within this study can be accessed at
688 <https://www.digitalrockportal.org/>.

689

690

References

- 691
692
693 Adler, P. M., and H. Brenner (1988), Multiphase flow in porous media, *Annual review of fluid mechanics*,
694 20(1), 35-59.
- 695 Al-Menhali, A. S., and S. Krevor (2016), Capillary Trapping of CO₂ in Oil Reservoirs: Observations in a
696 Mixed-Wet Carbonate Rock, *Environmental Science & Technology*, 50(5), 2727-2734.
- 697 Al-Menhali, A. S., H. P. Menke, M. J. Blunt, and S. C. Krevor (2016), Pore Scale Observations of Trapped
698 CO₂ in Mixed-Wet Carbonate Rock: Applications to Storage in Oil Fields, *Environmental Science*
699 & *Technology*, 50(18), 10282-10290.
- 700 Al-Raoush, R. I., Z. Abu-Salem, and C. S. Willson (2003), Characterization of non-wetting phase fluids in
701 porous media systems using high-resolution, three-dimensional, synchrotron X-ray
702 microtomography, *Abstracts of Papers of the American Chemical Society*, 225, 249-ENVR.
- 703 Al-Raoush, R. I., and C. S. Willson (2005a), A pore-scale investigation of a multiphase porous media
704 system, *Journal of Contaminant Hydrology*, 77(1-2), 67-89.
- 705 Al-Raoush, R. I., and C. S. Willson (2005b), Extraction of physically realistic pore network properties from
706 three-dimensional synchrotron X-ray microtomography images of unconsolidated porous media
707 systems, *Journal of Hydrology*, 300(1-4), 44-64.
- 708 Al-Raoush, R. I. (2009), Impact of Wettability on Pore-Scale Characteristics of Residual Nonaqueous
709 Phase Liquids, *Environmental Science & Technology*, 43(13), 4796-4801.
- 710 Alyafei, N., and M. J. Blunt (2016), The effect of wettability on capillary trapping in carbonates, *Advances*
711 *in Water Resources*, 90, 36-50.
- 712 Anderson, W. (1986a), Wettability Literature Survey- Part 2: Wettability Measurement.
- 713 Anderson, W. (1986b), Wettability Literature Survey- Part 1: Rock/Oil/Brine Interactions and the Effects
714 of Core Handling on Wettability.
- 715 Anderson, W. G. (1987a), Wettability Literature Survey Part 5: The Effects of Wettability on Relative
716 Permeability.
- 717 Anderson, W. G. (1987b), Wettability Literature Survey- Part 4: Effects of Wettability on Capillary
718 Pressure.
- 719 Andrew, M., B. Bijeljic, and M. J. Blunt (2013), Pore-scale imaging of geological carbon dioxide storage
720 under in situ conditions, *Geophysical Research Letters*, 40(15), 3915-3918.
- 721 Andrew, M., B. Bijeljic, and M. J. Blunt (2014a), Pore-scale imaging of trapped supercritical carbon
722 dioxide in sandstones and carbonates, *International Journal of Greenhouse Gas Control*, 22, 1-
723 14.
- 724 Andrew, M., B. Bijeljic, and M. J. Blunt (2014b), Pore-by-pore capillary pressure measurements using X-
725 ray microtomography at reservoir conditions: Curvature, snap-off, and remobilization of residual
726 CO₂, *Water Resources Research*, 50(11), 8760-8774.
- 727 Andrew, M., B. Bijeljic, and M. J. Blunt (2014c), Pore-scale contact angle measurements at reservoir
728 conditions using X-ray microtomography, *Advances in Water Resources*, 68, 24-31.
- 729 Andrew, M., B. Bijeljic, and M. Blunt (2015a), Reservoir Condition Pore-scale Imaging of Multiple Fluid
730 Phases Using X-ray Microtomography, *Journal of Visualized Experiments : JoVE*(96), 52440.
- 731 Andrew, M., H. Menke, M. J. Blunt, and B. Bijeljic (2015b), The Imaging of Dynamic Multiphase Fluid
732 Flow Using Synchrotron-Based X-ray Microtomography at Reservoir Conditions, *Transport in*
733 *Porous Media*, 110(1), 1-24.
- 734 Arif, M., A. Z. Al-Yaseri, A. Barifcani, M. Lebedev, and S. Iglauer (2016), Impact of pressure and
735 temperature on CO₂-brine-mica contact angles and CO₂-brine interfacial tension: Implications
736 for carbon geo-sequestration, *Journal of Colloid and Interface Science*, 462, 208-215.
- 737 Arif, M., M. Lebedev, A. Barifcani, and S. Iglauer (2017), CO₂ storage in carbonates: Wettability of
738 calcite, *International Journal of Greenhouse Gas Control*, 62, 113-121.

- 739 Beatty, S. M., and J. E. Smith (2010), Fractional wettability and contact angle dynamics in burned water
740 repellent soils, *Journal of Hydrology*, 391(1), 97-108.
- 741 Berg, S., et al. (2013), Real-time 3D imaging of Haines jumps in porous media flow, *Proceedings of the*
742 *National Academy of Sciences*, 110(10), 3755.
- 743 Berkowitz, B., and R. P. Ewing (1998), Percolation Theory and Network Modeling Applications in Soil
744 Physics, *Surveys in Geophysics*, 19(1), 23-72.
- 745 Bhattad, P., C. S. Willson, and K. E. Thompson (2010), Segmentation of low-contrast three-phase X-Ray
746 Computed Tomography images of porous media, paper presented at Proceedings of the GeoX
747 2010: 3rd International Workshop on X-ray CT for Geomaterials, New Orleans, LA.
- 748 Bikkina, P. K. (2011), Contact angle measurements of CO₂-water-quartz/calcite systems in the
749 perspective of carbon sequestration, *International Journal of Greenhouse Gas Control*, 5(5),
750 1259-1271.
- 751 Blunt, M. J., and H. Scher (1995), Pore-level modeling of wetting, *Physical Review E*, 52(6), 6387-6403.
- 752 Blunt, M. J. (1998), Physically-based network modeling of multiphase flow in intermediate-wet porous
753 media, *Journal of Petroleum Science and Engineering*, 20(3), 117-125.
- 754 Blunt, M. J., M. D. Jackson, M. Piri, and P. H. Valvatne (2002), Detailed physics, predictive capabilities
755 and macroscopic consequences for pore-network models of multiphase flow, *Advances in Water*
756 *Resources*, 25(8-12), 1069-1089.
- 757 Blunt, M. J., Q. Lin, T. Akai, and B. Bijeljic (2019), A thermodynamically consistent characterization of
758 wettability in porous media using high-resolution imaging, *Journal of Colloid and Interface*
759 *Science*, 552, 59-65.
- 760 Bradford, S. A., and L. M. Abriola (2001), Dissolution of residual tetrachloroethylene in fractional
761 wettability porous media: incorporation of interfacial area estimates, *Water Resources*
762 *Research*, 37(5), 1183-1195.
- 763 Broseta, D., N. Tonnet, and V. Shah (2012), Are rocks still water-wet in the presence of dense CO₂ or
764 H₂S?, *Geofluids*, 12(4), 280-294.
- 765 BROWN, K., S. SCHLÜTER, A. SHEPPARD, and D. WILDENSCHILD (2014), On the challenges of measuring
766 interfacial characteristics of three-phase fluid flow with x-ray microtomography, *Journal of*
767 *Microscopy*, 253(3), 171-182.
- 768 Bultreys, T., M. A. Boone, M. N. Boone, T. De Schryver, B. Masschaele, D. Van Loo, L. Van Hoorebeke,
769 and V. Cnudde (2015), Real-time visualization of Haines jumps in sandstone with laboratory-
770 based microcomputed tomography, *Water Resources Research*, 51(10), 8668-8676.
- 771 Chaudhary, K., M. Bayani Cardenas, W. W. Wolfe, J. A. Maisano, R. A. Ketcham, and P. C. Bennett (2013),
772 Pore-scale trapping of supercritical CO₂ and the role of grain wettability and shape, *Geophysical*
773 *Research Letters*, 40(15), 3878-3882.
- 774 Chiquet, P., D. Broseta, and S. Thibeau (2007), Wettability alteration of caprock minerals by carbon
775 dioxide, *Geofluids*, 7(2), 112-122.
- 776 Chomsurin, C., and C. J. Werth (2003), Analysis of pore-scale nonaqueous phase liquid dissolution in
777 etched silicon pore networks, *Water Resources Research*, 39(9).
- 778 Culligan, K. A., D. Wildenschild, B. S. B. Christensen, W. G. Gray, and M. L. Rivers (2006), Pore-scale
779 characteristics of multiphase flow in porous media: A comparison of air-water and oil-water
780 experiments, *Advances in Water Resources*, 29(2), 227-238.
- 781 Dawson, H. E., and P. V. Roberts (1997), Influence of Viscous, Gravitational, and Capillary Forces on
782 DNAPL Saturation, *Ground Water*, 35(2), 261-269.
- 783 Dixit, A. B., S. R. McDougall, K. S. Sorbie, and J. S. Buckley (1996), Pore Scale Modelling of Wettability
784 Effects and Their Influence on Oil Recovery, in *SPE/DOE Improved Oil Recovery Symposium*,
785 edited, Society of Petroleum Engineers, Tulsa, Oklahoma.

- 786 Dixit, A. B., J. S. Buckley, S. R. McDougall, and K. S. Sorbie (2000), Empirical Measures of Wettability in
787 Porous Media and the Relationship between Them Derived From Pore-Scale Modelling,
788 *Transport in Porous Media*, 40(1), 27-54.
- 789 Fenwick, D. H., and M. J. Blunt (1998), Three-dimensional modeling of three phase imbibition and
790 drainage, *Advances in Water Resources*, 21(2), 121-143.
- 791 Flury, M., and H. Qiu (2008), Modeling Colloid-Facilitated Contaminant Transport in the Vadose Zone,
792 *Vadose Zone Journal*, 7(2), 682-697.
- 793 Geistlinger, H., S. Mohammadian, S. Schlueter, and H.-J. Vogel (2014), Quantification of capillary
794 trapping of gas clusters using X-ray microtomography, *Water Resources Research*, 50(5), 4514-
795 4529.
- 796 Geistlinger, H., and I. Ataei-Dadavi (2015), Influence of the heterogeneous wettability on capillary
797 trapping in glass-beads monolayers: Comparison between experiments and the invasion
798 percolation theory, *Journal of Colloid and Interface Science*, 459, 230-240.
- 799 Geistlinger, H., I. Ataei-Dadavi, S. Mohammadian, and H.-J. Vogel (2015), The impact of pore structure
800 and surface roughness on capillary trapping for 2-D and 3-D porous media: Comparison with
801 percolation theory, *Water Resources Research*, 51(11), 9094-9111.
- 802 Geistlinger, H., and S. Mohammadian (2015), Capillary trapping mechanism in strongly water wet
803 systems: Comparison between experiment and percolation theory, *Advances in Water
804 Resources*, 79, 35-50.
- 805 Georgiadis, A., S. Berg, A. Makurat, G. Maitland, and H. Ott (2013), Pore-scale micro-computed-
806 tomography imaging: Nonwetting-phase cluster-size distribution during drainage and imbibition,
807 *Physical Review E*, 88(3), 033002.
- 808 Gershenson, N. I., R. W. Ritzi, D. F. Dominic, E. Mehnert, and R. T. Okwen (2017), Capillary trapping of
809 CO₂ in heterogeneous reservoirs during the injection period, *International Journal of
810 Greenhouse Gas Control*, 59(Complete), 13-23.
- 811 Haines, W. B. (1930), Studies in the physical properties of soil. V. The hysteresis effect in capillary
812 properties, and the modes of moisture distribution associated therewith, *The Journal of
813 Agricultural Science*, 20(1), 97-116.
- 814 Han, J., Y. Jin, and C. S. Willson (2006), Virus retention and transport in chemically heterogeneous
815 porous media under saturated and unsaturated flow conditions, *Environmental Science &
816 Technology*, 40(5), 1547-1555.
- 817 Heiba, A. A., G. R. Jerauld, H. T. Davis, and L. E. Scriven (1986), Mechanism-Based Simulation of Oil
818 Recovery Processes, in *SPE Annual Technical Conference and Exhibition*, edited, p. 16, Society of
819 Petroleum Engineers, New Orleans, Louisiana.
- 820 Herring, A. L., E. J. Harper, L. Andersson, A. Sheppard, B. K. Bay, and D. Wildenschild (2013), Effect of
821 fluid topology on residual nonwetting phase trapping: Implications for geologic CO₂
822 sequestration, *Advances in Water Resources*, 62, 47-58.
- 823 Herring, A. L., L. Andersson, S. Schlüter, A. Sheppard, and D. Wildenschild (2015), Efficiently engineering
824 pore-scale processes: The role of force dominance and topology during nonwetting phase
825 trapping in porous media, *Advances in Water Resources*, 79(0), 91-102.
- 826 Herring, A. L., A. Sheppard, L. Andersson, and D. Wildenschild (2016), Impact of wettability alteration on
827 3D nonwetting phase trapping and transport, *International Journal of Greenhouse Gas Control*,
828 46, 175-186.
- 829 Holtzman, R., and E. Segre (2015), Wettability Stabilizes Fluid Invasion into Porous Media via Nonlocal,
830 Cooperative Pore Filling, *Physical Review Letters*, 115(16), 164501.
- 831 Hou, B., Y. Wang, X. Cao, J. Zhang, X. Song, M. Ding, and W. Chen (2016), Mechanisms of Enhanced Oil
832 Recovery by Surfactant-Induced Wettability Alteration, *Journal of Dispersion Science and
833 Technology*, 37(9), 1259-1267.

- 834 Hsu, H.-L., and A. H. Demond (2007), Influence of Organic Acid and Organic Base Interactions on
835 Interfacial Properties in NAPL-Water Systems, *Environmental Science and Technology*, 41(3),
836 897-908.
- 837 Iglauer, S., A. Paluszny, C. H. Pentland, and M. J. Blunt (2011), Residual CO₂ imaged with X-ray micro-
838 tomography, *Geophysical Research Letters*, 38(21), n/a-n/a.
- 839 Iglauer, S., M. A. Fernø, P. Shearing, and M. J. Blunt (2012), Comparison of residual oil cluster size
840 distribution, morphology and saturation in oil-wet and water-wet sandstone, *Journal of Colloid
841 and Interface Science*, 375(1), 187-192.
- 842 Iglauer, S., C. H. Pentland, and A. Busch (2015), CO₂ wettability of seal and reservoir rocks and the
843 implications for carbon geo-sequestration, *Water Resources Research*, 51(1), 729-774.
- 844 Jadhunandan, P. P., and N. R. Morrow (1995), Effect of Wettability on Waterflood Recovery for Crude-
845 Oil/Brine/Rock Systems, *SPE Reservoir Engineering*, 10(01), 40-46.
- 846 Joekar-Niasar, V., and S. M. Hassanizadeh (2012), Analysis of Fundamentals of Two-Phase Flow in Porous
847 Media Using Dynamic Pore-Network Models: A Review, *Critical Reviews in Environmental
848 Science and Technology*, 42(18), 1895-1976.
- 849 Johnson, P. R., N. Sun, and M. Elimelech (1996), Colloid transport in geochemically heterogeneous
850 porous media: Modeling and measurements, *Environmental Science & Technology*, 30(11),
851 3284-3293.
- 852 Kamal, M. S., I. A. Hussein, and A. S. Sultan (2017), Review on Surfactant Flooding: Phase Behavior,
853 Retention, IFT, and Field Applications, *Energy & Fuels*, 31(8), 7701-7720.
- 854 Kennedy, H. T., E. O. Burja, and R. S. Boykin (1955), An investigation of the effects of wettability on oil
855 recovery by water flooding, *The Journal of Physical Chemistry*, 59(9), 867-869.
- 856 Kim, J.-W., D. Kim, and W. B. Lindquist (2013), A re-examination of throats, *Water Resources Research*,
857 49(11), 7615-7626.
- 858 Kovscek, A. R., H. Wong, and C. J. Radke (1993), A pore-level scenario for the development of mixed
859 wettability in oil reservoirs, *AIChE Journal*, 39(6), 1072-1085.
- 860 Krevor, S., R. Pini, L. Zuo, and S. M. Benson (2012), Relative permeability and trapping of CO₂ and water
861 in sandstone rocks at reservoir conditions, *Water Resources Research*, 48(2), n/a-n/a.
- 862 Krevor, S., M. J. Blunt, S. M. Benson, C. H. Pentland, C. Reynolds, A. Al-Menhali, and B. Niu (2015),
863 Capillary trapping for geologic carbon dioxide storage – From pore scale physics to field scale
864 implications, *International Journal of Greenhouse Gas Control*, 40, 221-237.
- 865 Kumar, M., M. A. Knackstedt, T. J. Senden, A. P. Sheppard, and J. P. Middleton (2010), Visualizing And
866 Quantifying the Residual Phase Distribution In Core Material.
- 867 Kumar, M., A. Fogden, T. Senden, and M. A. Knackstedt (2012), Investigation of Pore-Scale Mixed
868 Wettability.
- 869 Lemke, L. D., and L. M. Abriola (2006), Modeling dense nonaqueous phase liquid mass removal in
870 nonuniform formations: Linking source-zone architecture and system response, *Geosphere*, 2(2),
871 74-82.
- 872 Lenormand, R., C. Zarcone, and A. Sarr (1983), Mechanisms of the displacement of one fluid by another
873 in a network of capillary ducts, *Journal of Fluid Mechanics*, 135, 337-353.
- 874 Lenormand, R. (1986), Pattern growth and fluid displacements through porous media, *Physica A:
875 Statistical Mechanics and its Applications*, 140(1), 114-123.
- 876 Lenormand, R., E. Touboul, and C. Zarcone (1988), Numerical models and experiments on immiscible
877 displacements in porous media, *Journal of Fluid Mechanics*, 189, 165-187.
- 878 Lord, D. L. (1999), Influence of organic acid and base solution chemistry on interfacial and transport
879 properties of mixed wastes in the subsurface, Ph.D. thesis, 190 pp, University of Michigan,
880 United States -- Michigan.

- 881 Melrose, J. C., and C. F. Brandner (1974), Role of Capillary Forces In Detennining Microscopic
882 Displacement Efficiency For Oil Recovery By Waterflooding.
- 883 Molnar, I. L., D. M. O'Carroll, and J. I. Gerhard (2011), Impact of surfactant-induced wettability
884 alterations on DNAPL invasion in quartz and iron oxide-coated sand systems, *Journal of*
885 *Contaminant Hydrology*, 119(1-4), 1-12.
- 886 Morrow, N. R. (1976), Capillary Pressure Correlations For Uniformly Wetted Porous Media.
- 887 Morrow, N. R. (1990), Wettability and Its Effect on Oil Recovery, *Journal of Petroleum Technology*, 1476-
888 1484.
- 889 Nambi, I. M., and S. E. Powers (2000), NAPL dissolution in heterogeneous systems: an experimental
890 investigation in a simple heterogeneous system, *Journal of Contaminant Hydrology*, 44(2), 161-
891 184.
- 892 Norouzi Rad, M., N. Shokri, and M. Sahimi (2013), Pore-scale dynamics of salt precipitation in drying
893 porous media, *Physical Review E*, 88(3), 032404.
- 894 Oh, W., and W. B. Lindquist (1999), Image thresholding by indicator kriging, *Ieee Transactions on Pattern*
895 *Analysis and Machine Intelligence*, 21(7), 590-602.
- 896 Oren, P. E., S. Bakke, and O. J. Arntzen (1998), Extending Predictive Capabilities to Network Models.
- 897 Oren, P. E., and S. Bakke (2003), Reconstruction of Berea sandstone and pore-scale modelling of
898 wettability effects, *Journal of Petroleum Science and Engineering*, 39(3-4), 177-199.
- 899 Pentland, C. H., R. El-Maghraby, S. Iglauer, and M. J. Blunt (2011), Measurements of the capillary
900 trapping of super-critical carbon dioxide in Berea sandstone, *Geophysical Research Letters*,
901 38(6), n/a-n/a.
- 902 Phelan, T. J., L. D. Lemke, S. A. Bradford, D. M. O'Carroll, and L. M. Abriola (2004), Influence of textural
903 and wettability variations on predictions of DNAPL persistence and plume development in
904 saturated porous media, *Advances in Water Resources*, 27(4), 411-427.
- 905 Porter, M. L., D. Wildenschild, G. Grant, and J. I. Gerhard (2010), Measurement and prediction of the
906 relationship between capillary pressure, saturation, and interfacial area in a NAPL-water-glass
907 bead system, *Water Resources Research*, 46(8), n/a-n/a.
- 908 Powers, S. E., W. H. Anckner, and T. H. Seacord (1996), Wettability of NAPL-Contaminated Sands, *Journal*
909 *of Environmental Engineering*, 122(10), 889-896.
- 910 Powers, S. E., I. M. Nambi, and G. W. Curry (1998), Non-aqueous phase liquid dissolution in
911 heterogeneous systems: Mechanisms and a local equilibrium modeling approach, *Water*
912 *Resources Research*, 34(12), 3293-3302.
- 913 Rabbani, H. S., V. Joekar-Niasar, T. Pak, and N. Shokri (2017), New insights on the complex dynamics of
914 two-phase flow in porous media under intermediate-wet conditions, *Scientific Reports*, 7(1),
915 4584.
- 916 Rabbani, H. S., B. Zhao, R. Juanes, and N. Shokri (2018), Pore geometry control of apparent wetting in
917 porous media, *Scientific Reports*, 8(1), 15729.
- 918 Rivers, M. L., D. T. Citron, and Y. B. Wang (2010), Recent developments in computed tomography at
919 GSECARS, in *Developments in X-Ray Tomography VII*, edited by S. R. Stock, Spie-Int Soc Optical
920 Engineering, Bellingham.
- 921 Rucker, M., et al. (2015), From connected pathway flow to ganglion dynamics, *Geophysical Research*
922 *Letters*, 42(10), 3888-3894.
- 923 Ryder, J. L., and A. H. Demond (2008), Wettability hysteresis and its implications for DNAPL source zone
924 distribution, *Journal of Contaminant Hydrology*, 102(1-2), 39-48.
- 925 Salathiel, R. A. (1973), Oil Recovery by Surface Film Drainage In Mixed-Wettability Rocks.
- 926 Scheidegger, A. (1958), *The physics of flow through porous media*, University Of Toronto Press: London.

- 927 Schnaar, G., and M. L. Brusseau (2005), Pore-scale characterization of organic immiscible-liquid
928 morphology in natural porous media using synchrotron X-ray microtomography, *Environmental*
929 *Science & Technology*, 39(21), 8403-8410.
- 930 Schnaar, G., and M. L. Brusseau (2006), Characterizing pore-scale dissolution of organic immiscible liquid
931 in natural porous media using synchrotron X-ray microtomography, *Environmental Science &*
932 *Technology*, 40(21), 6622-6629.
- 933 Schroth, M. H., J. D. Istok, S. J. Ahearn, and J. S. Selker (1996), Characterization of Miller-Similar Silica
934 Sands for Laboratory Hydrologic Studies, *Soil Science Society of America Journal*, 60(5), 1331-
935 1339.
- 936 Shahraeeni, E., and D. Or (2010), Pore-Scale Analysis of Evaporation and Condensation Dynamics in
937 Porous Media, *Langmuir*, 26(17), 13924-13936.
- 938 Shokri, N., P. Lehmann, P. Vontobel, and D. Or (2008), Drying front and water content dynamics during
939 evaporation from sand delineated by neutron radiography, *Water Resources Research*, 44(6),
940 n/a-n/a.
- 941 Shokri, N., P. Lehmann, and D. Or (2009), Characteristics of evaporation from partially wettable porous
942 media, *Water Resources Research*, 45(2), n/a-n/a.
- 943 Singh, K., B. Bijeljic, and M. J. Blunt (2016), Imaging of oil layers, curvature and contact angle in a mixed-
944 wet and a water-wet carbonate rock, *Water Resources Research*, 52(3), 1716-1728.
- 945 Sirivithayapakorn, S., and A. Keller (2003), Transport of colloids in unsaturated porous media: A pore-
946 scale observation of processes during the dissolution of air-water interface, *Water Resources*
947 *Research*, 39(12).
- 948 Stauffer, F. (1978), Time dependence of the relations between capillary pressure, water content and
949 conductivity during drainage of porous media, paper presented at IAHR symposium on scale
950 effects in porous media, Thessaloniki, Greece.
- 951 Sweijen, T., E. Nikooee, S. M. Hassanizadeh, and B. Chareyre (2016), The Effects of Swelling and Porosity
952 Change on Capillarity: DEM Coupled with a Pore-Unit Assembly Method, *Transport in Porous*
953 *Media*, 113(1), 207-226.
- 954 Sweijen, T., H. Aslannejad, and S. M. Hassanizadeh (2017), Capillary pressure–saturation relationships
955 for porous granular materials: Pore morphology method vs. pore unit assembly method,
956 *Advances in Water Resources*, 107, 22-31.
- 957 Sweijen, T., S. M. Hassanizadeh, B. Chareyre, and L. Zhuang (2018), Dynamic Pore-Scale Model of
958 Drainage in Granular Porous Media: The Pore-Unit Assembly Method, *Water Resources*
959 *Research*, 54(6), 4193-4213.
- 960 Thompson, K. E., C. S. Willson, and W. L. Zhang (2006), Quantitative computer reconstruction of
961 particulate materials from microtomography images, *Powder Technology*, 163(3), 169-182.
- 962 Thompson, K. E., C. S. Willson, C. D. White, S. L. Nyman, J. P. Bhattacharya, and A. H. Reed (2008),
963 Application of a new grain-based reconstruction algorithm to microtomography images for
964 quantitative characterization and flow modeling, *Spe Journal*, 13(2), 164-176.
- 965 Ustohal, P., F. Stauffer, and T. Dracos (1998), Measurement and modeling of hydraulic characteristics of
966 unsaturated porous media with mixed wettability, *Journal of Contaminant Hydrology*, 33(1), 5-
967 37.
- 968 Wan, J., and T. K. Tokunaga (1997), Film Straining of Colloids in Unsaturated Porous Media: Conceptual
969 Model and Experimental Testing, *Environmental Science & Technology*, 31(8), 2413-2420.
- 970 Wildenschild, D., J. W. Hopmans, M. L. Rivers, and A. J. R. Kent (2005), Quantitative Analysis of Flow
971 Processes in a Sand Using Synchrotron-Based X-ray Microtomography, *Vadose Zone Journal*,
972 4(1), 112-126.
- 973 Wilkinson, D., and J. F. Willemsen (1983), Invasion percolation: a new form of percolation theory,
974 *Journal of Physics A: Mathematical and General*, 16(14), 3365.

975 Zhang, C., M. Oostrom, T. W. Wietsma, J. W. Grate, and M. G. Warner (2011), Influence of Viscous and
976 Capillary Forces on Immiscible Fluid Displacement: Pore-Scale Experimental Study in a Water-
977 Wet Micromodel Demonstrating Viscous and Capillary Fingering, *Energy & Fuels*, 25(8), 3493-
978 3505.

979 Zhao, B., C. W. MacMinn, and R. Juanes (2016), Wettability control on multiphase flow in patterned
980 microfluidics, *Proceedings of the National Academy of Sciences*, 113(37), 10251-10256.

981

982

983 *Table 1: Overview of PCE/water/surface contact angles¹*

Parameter	WW Sand	IW Sand
Surface type	Iron Oxide	Quartz
Smooth plate contact angle (°) ²	25	160
Operative contact angle (°) ^{2,3}	<1	63

984 ¹ From Molnar et al [2011]985 ² Reported through water phase during NAPL advancement/water drainage986 ³ Determined by Leverett-scaling capillary pressure-saturation relationships

987

988 *Table 2: Overview of extracted pore network and pore topological characteristics*

Parameter	WW Sand	IW Sand
Porosity (%)	41	33
# pores	17,383	17,836
# throats	114,722	102,563
Avg. pore connectivity ¹	6.6	5.7
Avg. PIR ² (cm)	0.0057	0.0057

989 ¹The average number of pores connected to a single pore body990 ² Pore Inscribed Radius (PIR) is the radius of the largest sphere that can be drawn within a
991 pore [Thompson et al., 2006]

992

993 *Table 3: Percentage of NAPL-occupied pores in WW and IW sands sorted by pore size*

	Large pores (PIR > 0.01 cm)		Medium pores (PIR: 0.005–0.01 cm)		Small pores (PIR < 0.005cm)	
	WW	IW	WW	IW	WW	IW
Top	98	95	74	65	6.3	4.3
Middle	100	100	98	88	12	13
Bottom	100	100	99	94	9.0	20

994

995 Figure 1: (a) Pore-size distribution by percentage of number of pores, (b) Throat-size distribution
996 by percentage of throats for water wetting (WW, purple) and intermediate wetting sands (IW,
997 black), (c) A representative slice illustrating pore bodies identified from the pore network
998 extraction algorithm for the intermediate-wetting sand (i.e., quartz sand). Each colour represents
999 a single uniquely identified pore body.

1000 Figure 2: Representative vertical cross-sections of (A) intermediate-wetting and (B) water-
1001 wetting systems after injecting 150 and 200 μL of NAPL respectively. In the images

1002 white=NAPL, gray=sand, black=water. (D) and (D): Magnified views of the outlined sections in
1003 images (A) and (B).

1004 Figure 3: NAPL saturations ($S_{N,p}$) for every individual pore body as a function of each pore's
1005 height within the dataset (h_{bi}) for the (a) WW and (b) IW systems. Each dot represents 1 pore.
1006 Best fit linear trendlines are overlain on each plot alongside the fitted equations describing how
1007 $S_{N,p}$ changes with height.

1008 Figure 4: Histograms of pore NAPL saturations for NAPL-occupied pores at selected heights
1009 (see Fig's 3a and 3b) for the water wetting and intermediate wetting experiments.

1010 Figure 5: The relationship between a pore body's inscribed radius (x-axis) and the radius of the
1011 pore's largest throat (y-axis) for water wetting (WW, left) and intermediate wetting (IW, right)
1012 sands. Each data point represents a single pore body. Blue data-points represent water-occupied
1013 pores and red data-points represent NAPL-occupied pores where NAPL saturation > 20%.

1014 Figure 6: Pore phase occupancy as a function of pore inscribe radii and vertical height for a)
1015 WW and b) IW sands. Each blue dot represents an individual pore with > 80% water saturation.
1016 Each red dot represents an individual pore with >20% NAPL saturation. Only water-occupied
1017 pores that are immediately adjacent to at least one NAPL-occupied pore are shown.

1018 Figure 7: Histograms of pore phase-occupancy vs pore inscribed radii for select height intervals
1019 in a) WW and b) IW sands. Histograms of the pore inscribed radii for all considered pores
1020 (NAPL- + water-occupied pores) are overlain on each height interval (black line).

1021

Figure 1.

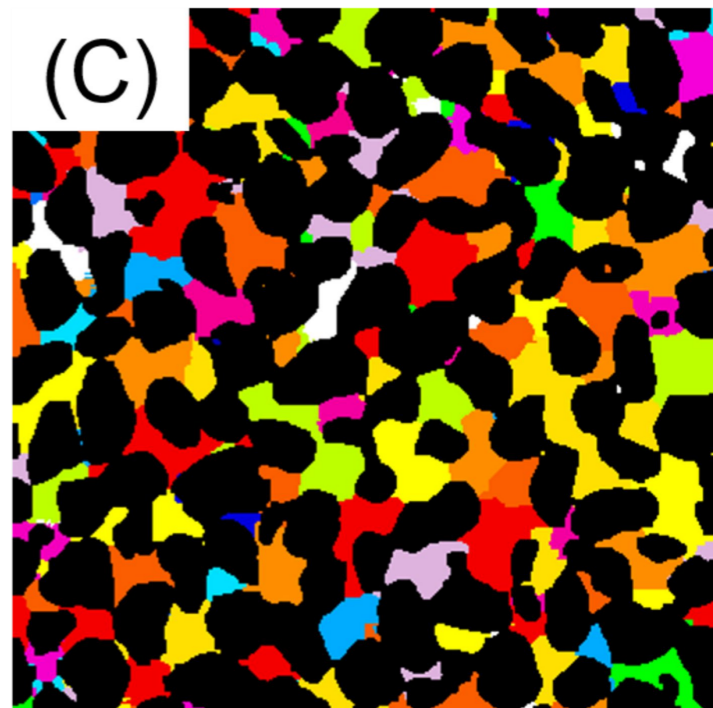
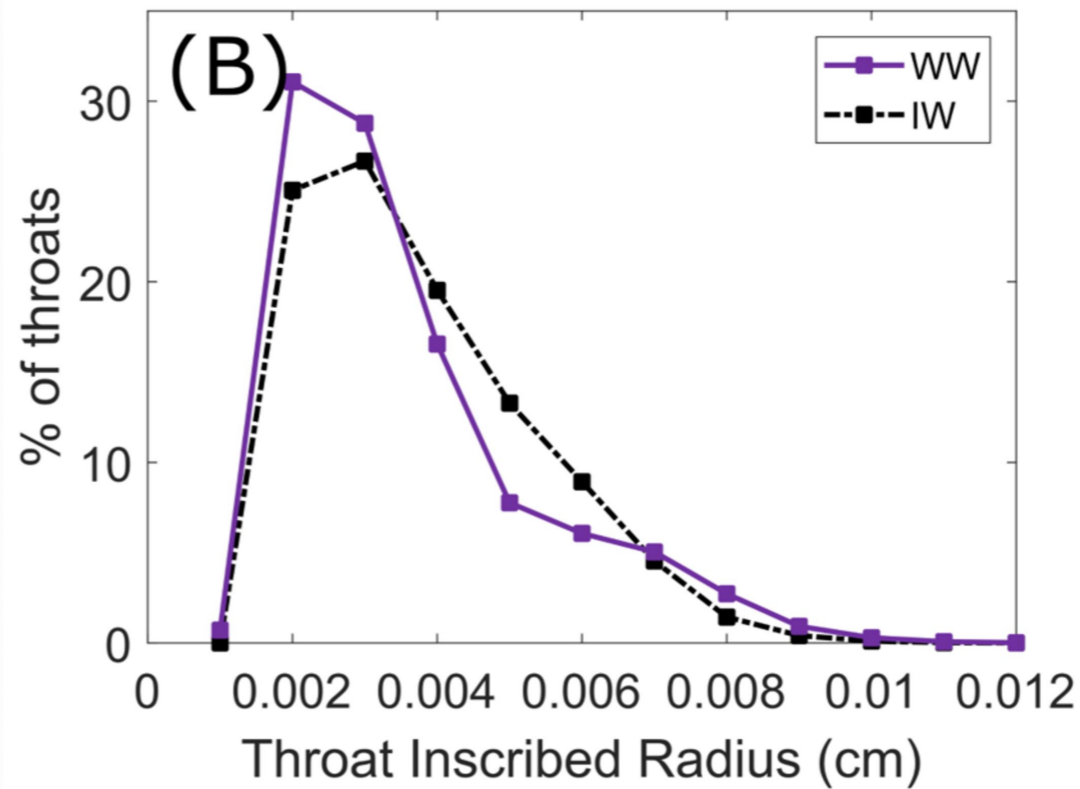
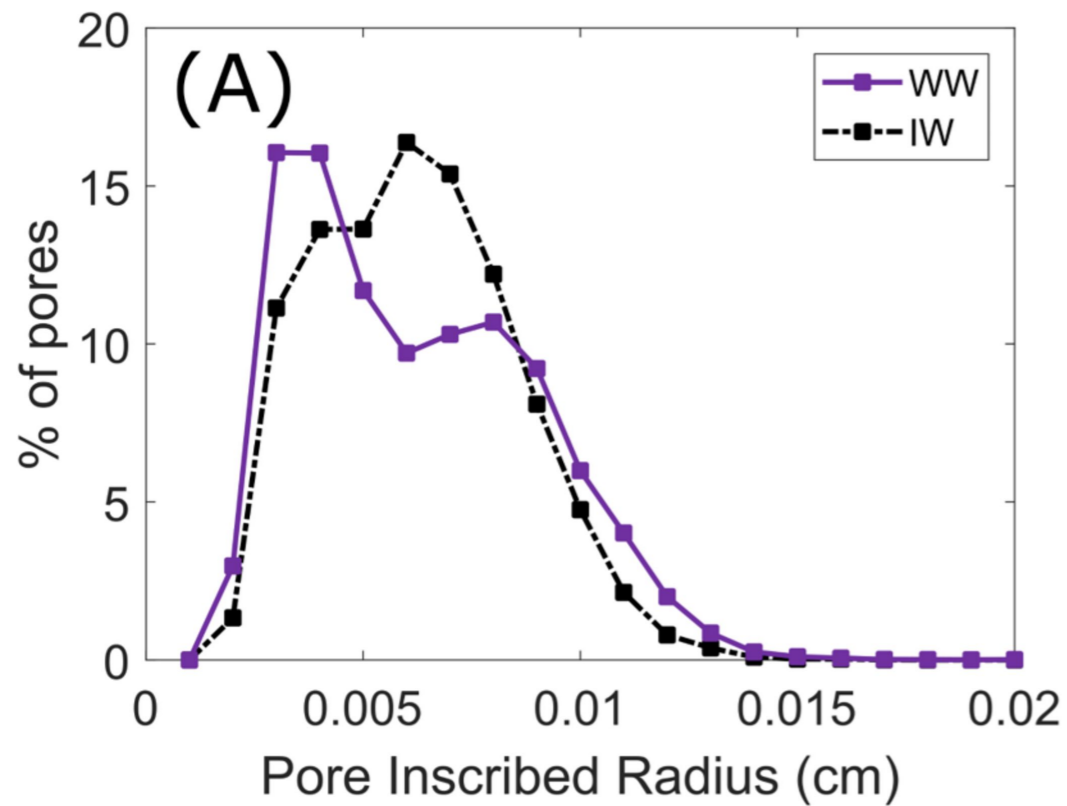
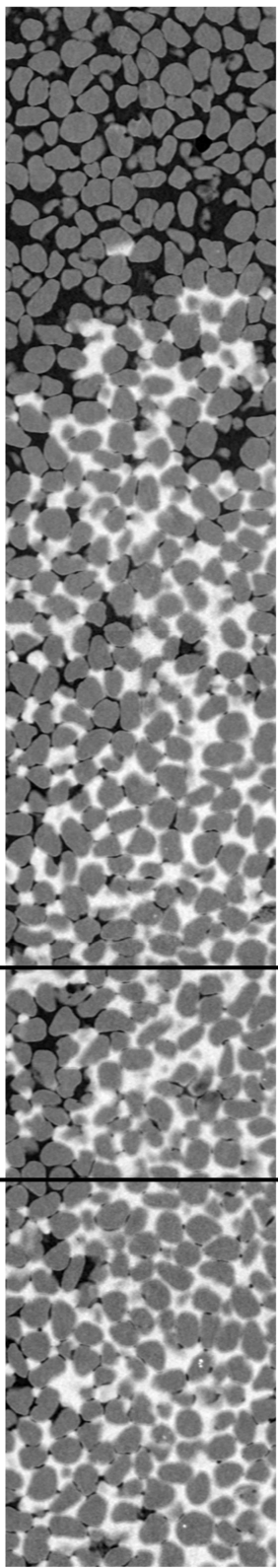
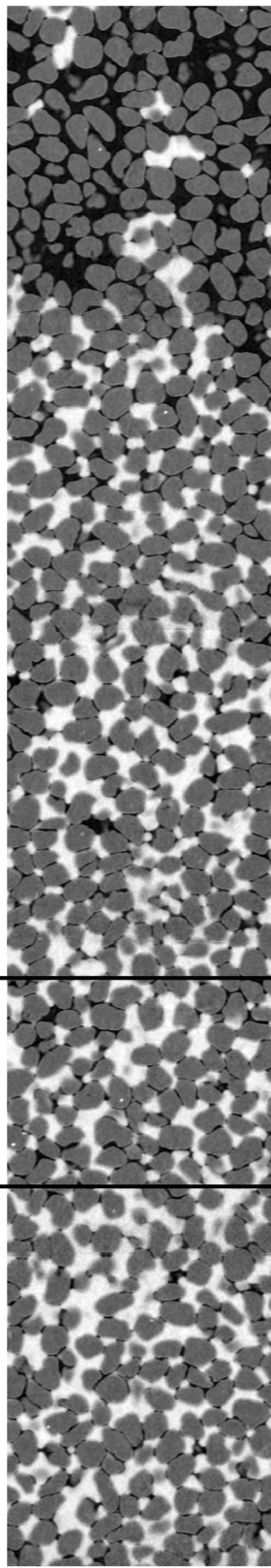


Figure 2.

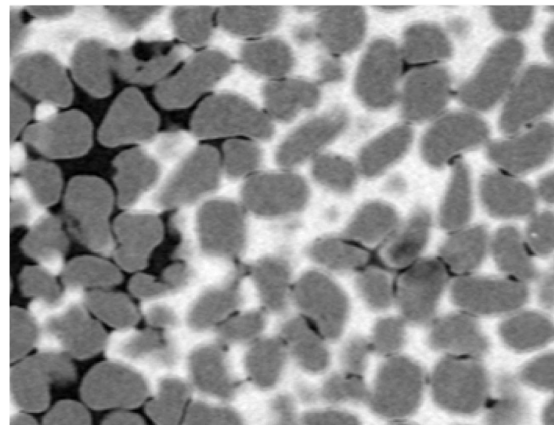
(A) Quartz:
Intermediate Wetting (IW)



(B) Iron Oxide:
Water Wetting (WW)



(C) IW magnified



(D) WW magnified

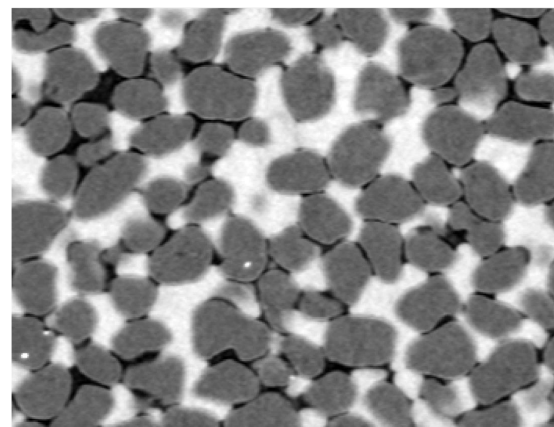
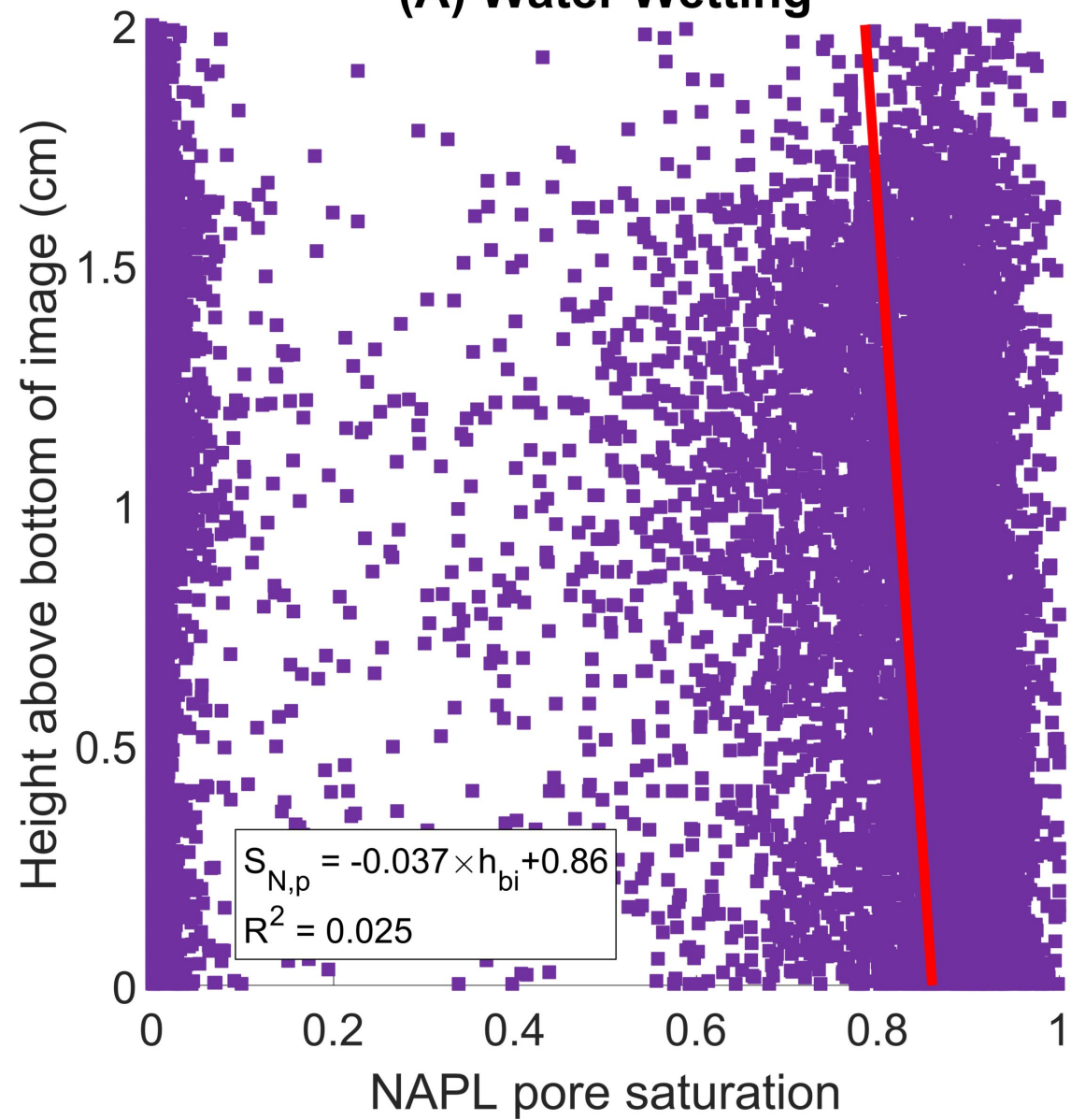


Figure 3.

(A) Water Wetting



(B) Intermediate Wetting

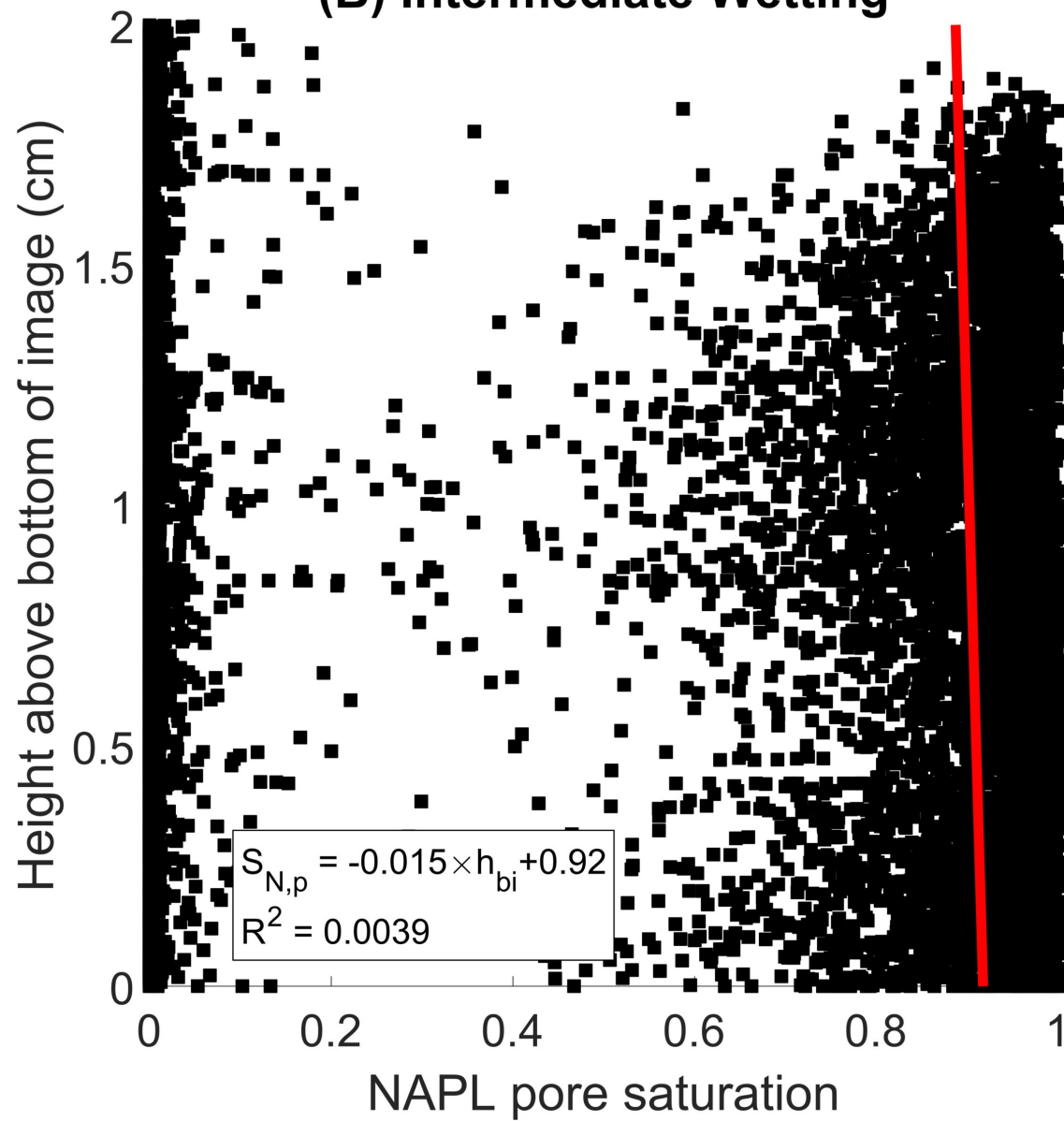


Figure 4.

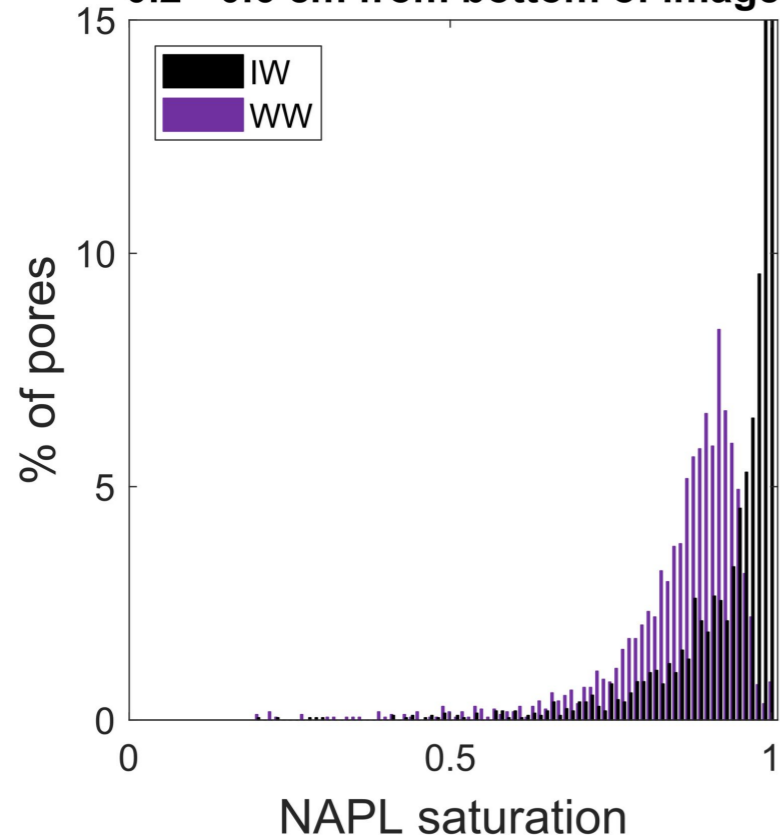
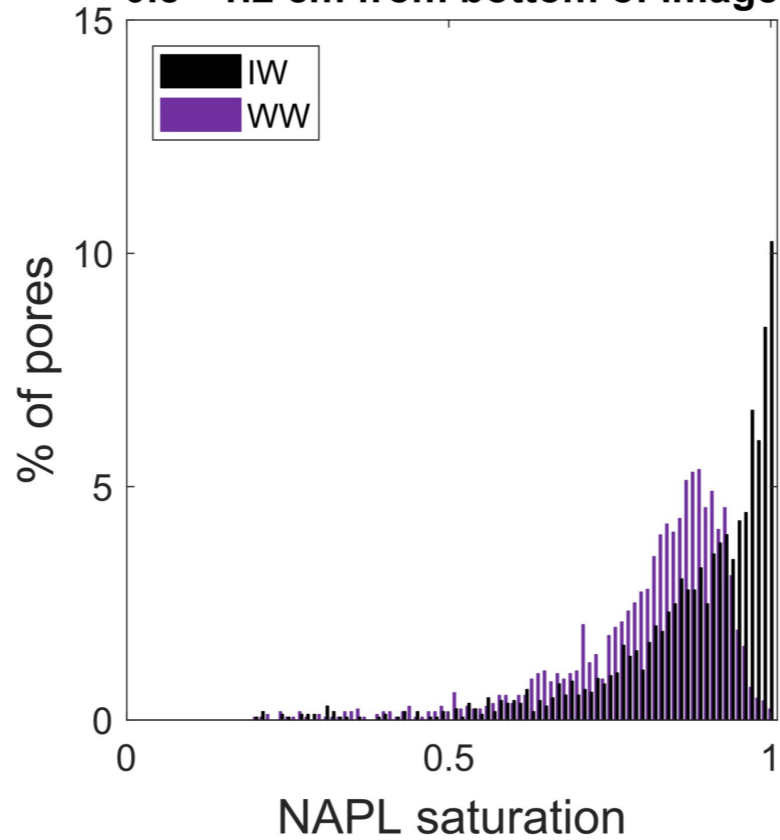
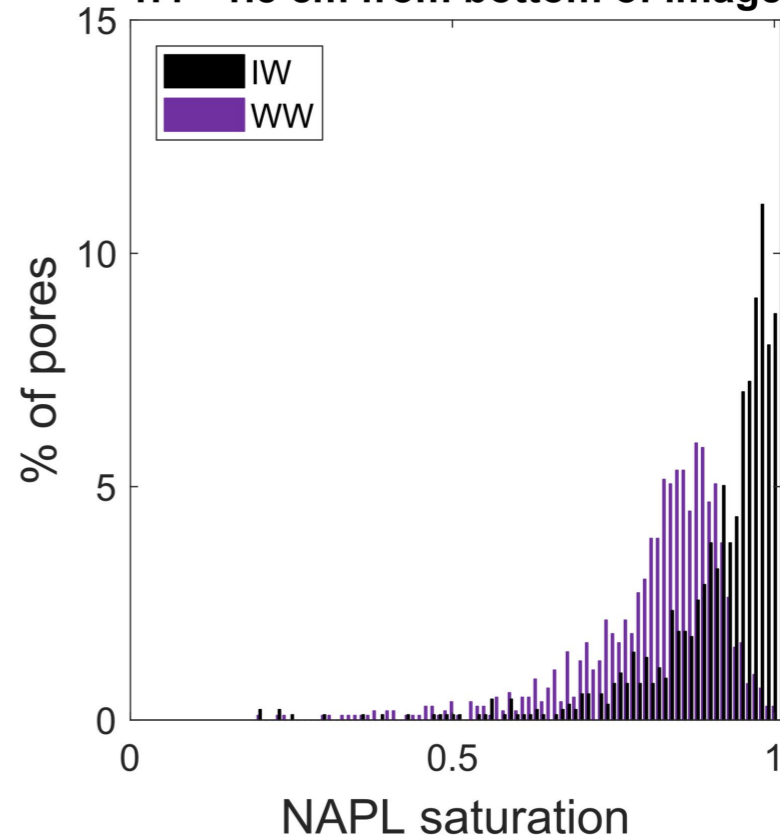
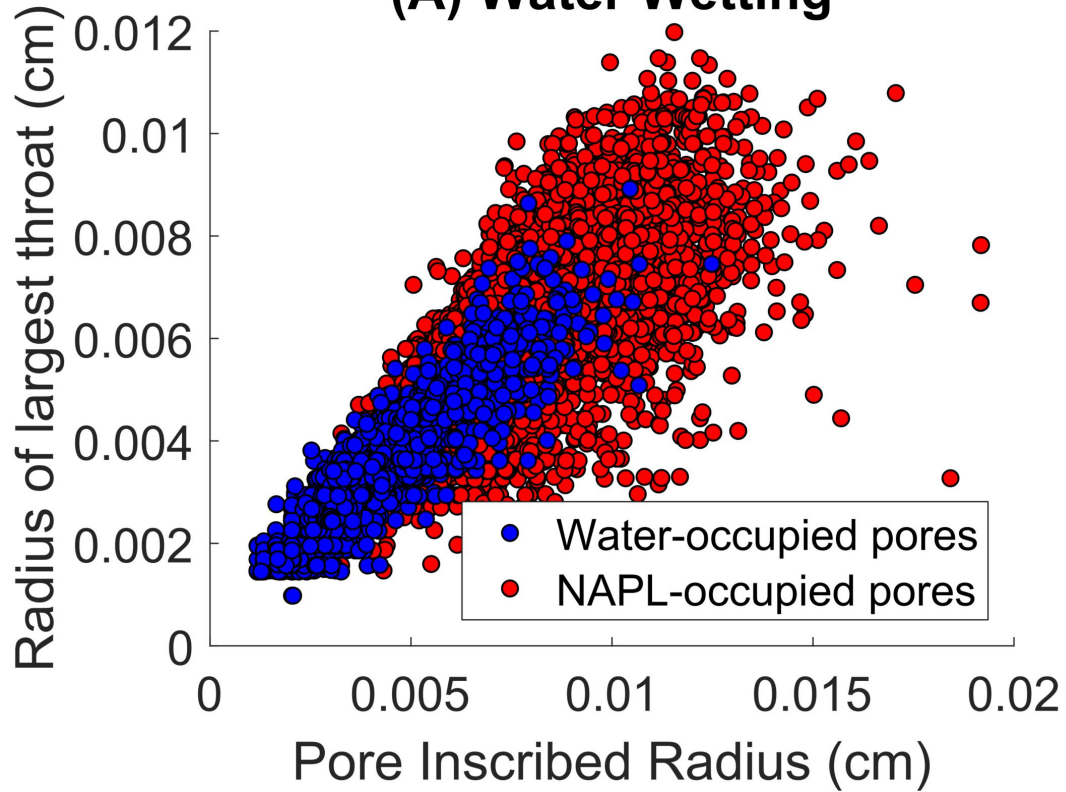
0.2 - 0.6 cm from bottom of image**0.8 - 1.2 cm from bottom of image****1.4 - 1.8 cm from bottom of image**

Figure 5.

(A) Water Wetting



(B) Intermediate Wetting

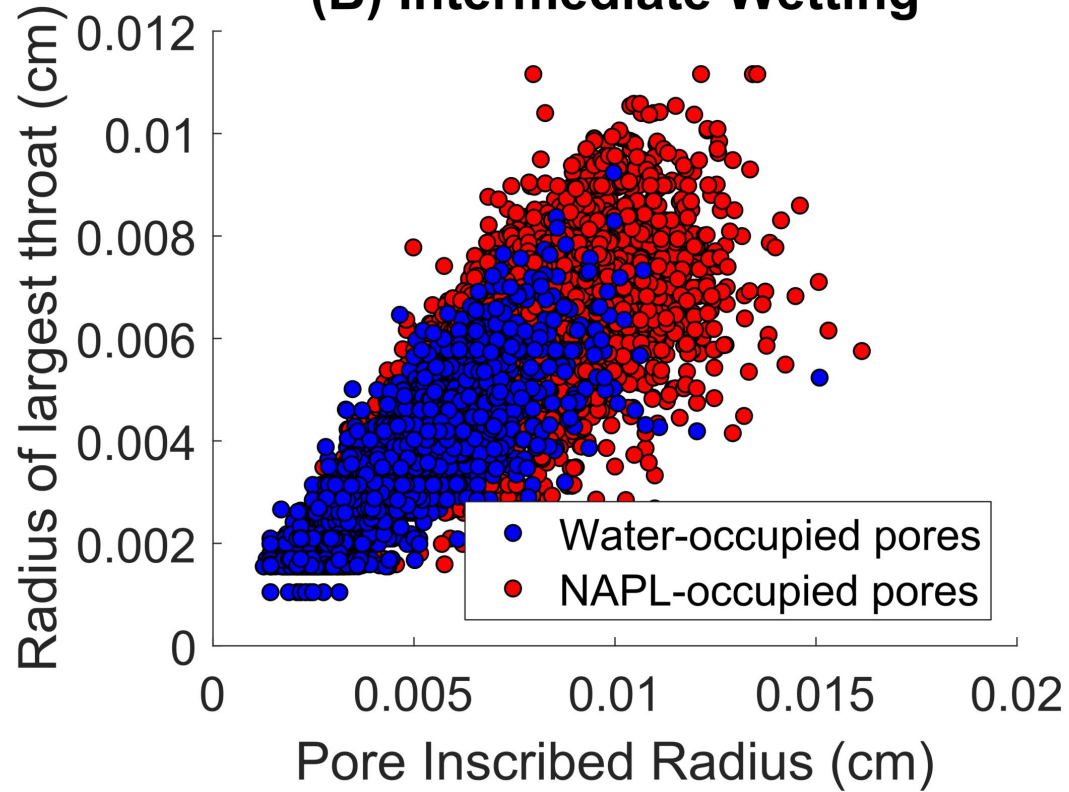
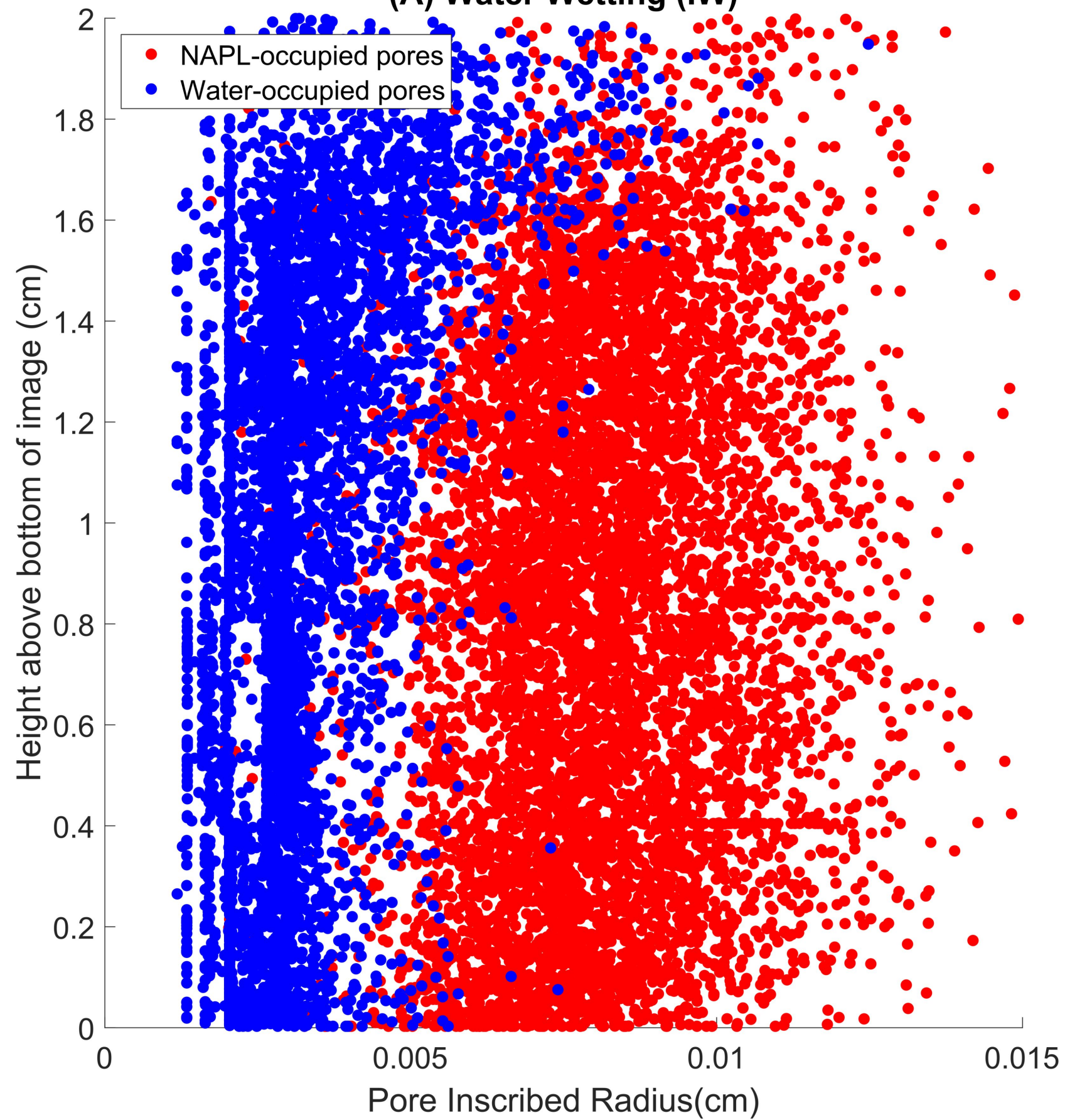


Figure 6.

(A) Water Wetting (IW)



(B) Intermediate Wetting (IW)

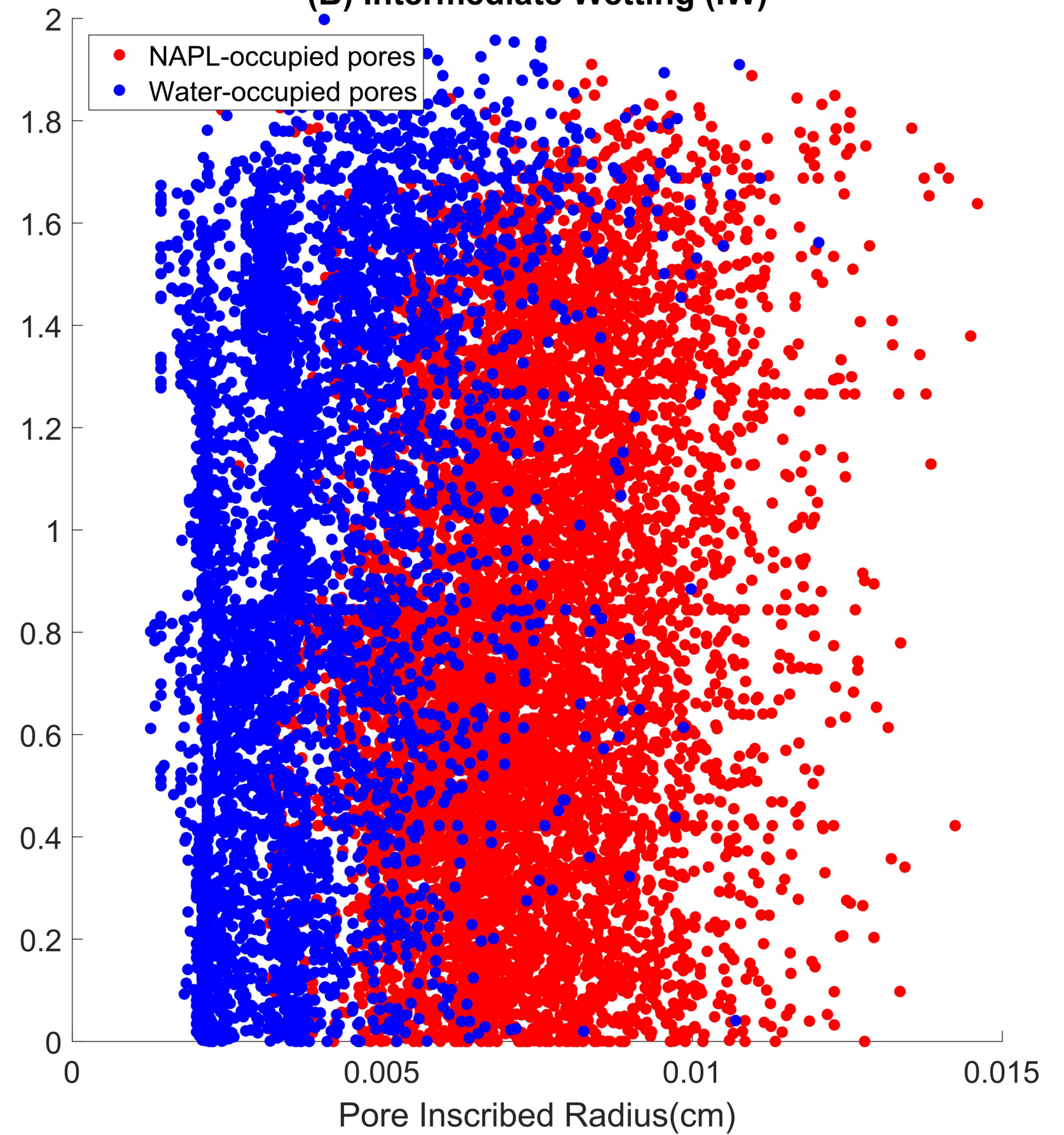
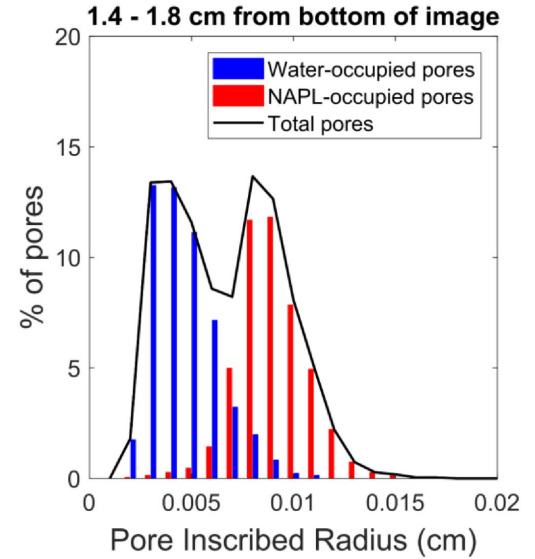
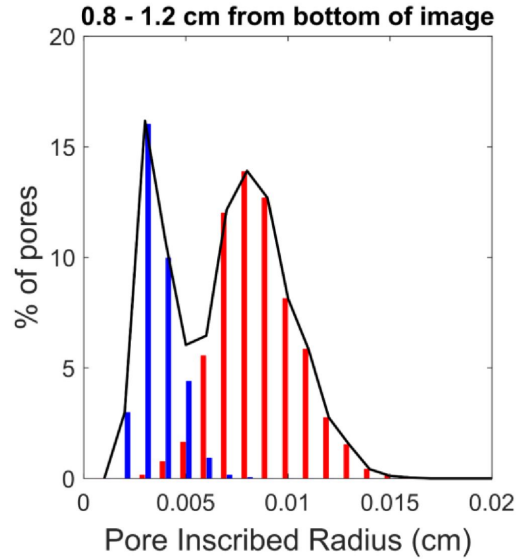
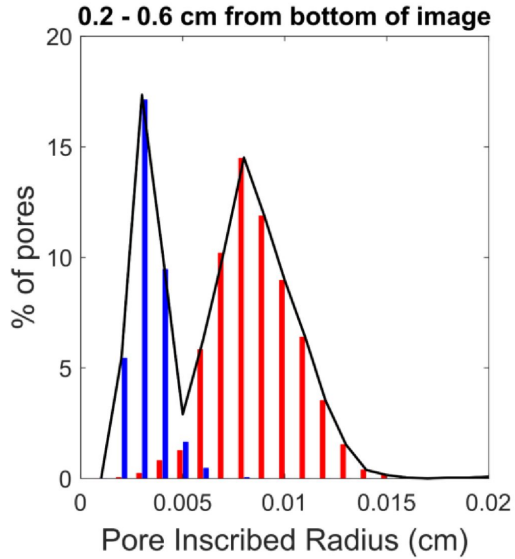


Figure 7.

Water Wetting (WW)



Intermediate Wetting (IW)

